

Review Article

A Gradient Stable Node-Based Smoothed Discrete Shear Gap Method for Analysis of Reissner–Mindlin Plates

Yadong Xu,¹ Guangsong Chen ,^{1,2} and Jinsong Tang¹

¹School of Mechanical Engineering, Nanjing University of Science and Technology, Nanjing 210094, China

²Nanjing University of Science and Technology, Changshu Research Institute Co., Ltd., Suzhou 215500, China

Correspondence should be addressed to Guangsong Chen; cgsnjst@njst.edu.cn

Received 31 March 2020; Revised 27 May 2020; Accepted 15 June 2020; Published 27 August 2020

Academic Editor: Marco Lepidi

Copyright © 2020 Yadong Xu et al. This is an open access article distributed under the Creative Commons Attribution License, which permits unrestricted use, distribution, and reproduction in any medium, provided the original work is properly cited.

In this paper, a gradient stable node-based smoothed discrete shear gap method (GS-DSG) using 3-node triangular elements is presented for Reissner–Mindlin plates in elastic-static, free vibration, and buckling analyses fields. By applying the smoothed Galerkin weak form, the discretized system equations are obtained. In order to carry out the smoothing operation and numerical integration, the smoothing domain associated with each node is defined. The modified smoothed strain with gradient information is derived from the Hu–Washizu three-field variational principle, resulting in the stabilization terms in the system equations. The stabilized discrete shear gap method is also applied to avoid transverse shear-locking problem. Several numerical examples are provided to illustrate the accuracy and effectiveness. The results demonstrate that the presented method is free of shear locking and can overcome the temporal instability issues, simultaneously obtaining excellent solutions.

1. Introduction

Thin-walled structures (shells) render a majority of engineering structures, and as one special case of shells, the plate has been widely used in mechanical, civil, marine, aerospace, and other engineering science fields. The analyses of plate structures in elastic-static, free vibration, and buckling fields stand for the key three aspects in their engineering application. There exist two first-order plate theories, namely, the Kirchhoff plate theory and the Reissner–Mindlin one. Kirchhoff theory is usually applied to thin structures with negligible shear strain, and the C^1 -continuous shape function is required. In view of its simplicity and efficiency, the lower-order Reissner–Mindlin plate which considered the shear effects is appealing in practical and only requires the C^0 -continuity shape function for both translational and rotational displacement fields. However, the shear-locking phenomenon of Reissner–Mindlin plate elements emerges when the thickness reaches the thin limit, and this is due to spurious transverse shear strains/stresses in bending. A development residing on node-based kinematics that aims at alleviation of the shear-locking effect and local improvement

of stress recovery has been recently presented by Valvano et al. [1] Besides, many researchers proposed large amounts of effective elements to address this difficulty, such as the assumed natural discrete shear gap (DSG) method [2–5], strain (ANS) methods [6, 7], and also the methods in [8–16]. All the methods show excellent performance in reducing the shear-locking deficiency and increasing the solution accuracy. The DSG method, similar to the ANS method, owns a property of “glue” because of no additional collocation points and fits the combination with other novel element techniques. Marinkovic et al. [17], applies DSG for the plate part of a flat shell element together with a strain smoothing technique implemented so as to make it independent from node numbering, and it was made available to users through ABAQUS implementation of the element.

Up to now, the finite element method (FEM) still holds its place as the most widely used numerical tool to simulate different behaviors of plates [18, 19] and other structures due to its robustness, reliability, and effectiveness. Unlike traditional FEM in which element connectivity should be established to form the discretized equations, another form of numerical method development called the meshfree or

meshless method [20–44] has attracted much attention. Regardless of the element connectivity among the nodes and mesh, only a set of nodes scattered in the problem domain are required. Although the meshfree indeed can overcome some drawbacks of FEM, it still cannot overcome all the deficiencies of FEM. Some key limitations are the difficulties in essential boundary condition implementation, high computational cost, and overly complex trial function construction processes. In an effort to make use of both advantages of FEM and meshless methods, Liu et al. have extended the concept of smoothing domains to formulate a family of smoothed finite element methods (SFEM) [45–47] by using the strain smoothing technique [48]. Researchers further proposed the edge-based smoothed finite element method (ES-FEM) [49] and node-based smoothed finite element method (NS-FEM) [50] based on the concept of SFEM.

NS-FEM can be regarded as a modified model of FEM. It has very attractive properties and can be easily applied to tetrahedral or triangular elements without any modification of formulas and procedures. NS-FEM wins the favor recently for its prominent inherent properties [51], such as its insensitivity to element distortion and its immunity to volumetric locking. Moreover, the computation efficiency of NS-FEM has been studied in previous works using bandwidth solvers for linear elastic-statics [52, 53]. It is, however, found that the NS-FEM behaves “overly soft” resulting from correction to the “overly stiff” behavior of the compatible FEM. Such an “overly soft” behavior leads to the so-called temporal instability [54]. In addition, spatial instability, another kind of instability, is also a common problem in node integration. The spatial instability can be successfully eliminated by smoothing operation. Temporal instability can be reflected in the modal frequency analysis of structures, which often leads to spurious nonzero energy modes in free vibration analyses and is still a problem to be solved. In [55], Beissel and Belytschko pointed out that by adding a stabilization term that contains the square of the residual of the equilibrium equation to the potential energy functional, the problem of nodal integration which suffers from spurious single modes due to underintegration of the weak form can be solved. Chai et al. [56] also proposed a stable NS-FEM to cure the “overly soft” of NS-FEM for analysis of underwater acoustic scattering problems. To overcome temporal instability of nodal integration in metal-forming simulations, Bonet and Kulasegaram [57] presented a least-square stabilization procedure based on these previous works, and Zhang and Liu [53] further developed a stabilization procedure for NS-FEM and then provided a recommended range for the stabilization parameter. By expanding the Taylor series of the function of the displacement field [58], it can be used to reduce the instability in direct node integration. However, since the high-order derivatives appear in underlying formulations, the computational cost will increase. Other forms of stabilization consisting of the Taylor expansion and displacement smoothing have been proposed

[59], wherein the nodal integration technique is directly applied to obtain stable solutions. Puso et al. [60] developed a nodal integration technique by adding integration points, of which the effectiveness has been proved for both small and large deformation problems. Feng et al. [61] proposed a stable nodal integration method with strain gradient for dynamic analyses of solid structures based on NS-FEM. The proposed method can achieve appropriate system stiffness in train energy between FEM and NS-FEM solutions and indeed provide temporally stable results. There still exist a variety of gradient term constructions available for different cases [37, 40, 62–67].

In this work, a gradient stable node-based smoothed discrete shear gap method (GS-DSG) using 3-node triangular elements is formulated for elastic-static, free vibration, and buckling analyses of Reissner–Mindlin plates. In order to overcome the temporal instability problem encountered in the nodal integration process, the smoothed Galerkin weak form is applied by using the strain smoothing technique with gradient information, which is derived from the Hu–Washizu three-field variation principle. The stabilized discrete shear gap method is also incorporated into the presented method to avoid the transverse shear locking and improve the accuracy of the present formulation. The numerical examples presented herein demonstrate that the present method is both free of shear locking and temporal instability. It also achieves high accuracy compared with the exact solutions and other existing methods in the literature.

The outline of this paper is as follows. Section 2 describes the weak form of the governing equations and the formulation of the 3-node plate element. In Section 3, the gradient stable integration formulation for Reissner–Mindlin plates with the stabilized discrete shear gap technique is introduced. Section 4 demonstrates the effectiveness of the presented method through numerical examples. Finally, the paper closes with concluding remarks.

2. Theoretical Formulations

2.1. Basic Equations for Reissner–Mindlin Plates. Based on the assumption of the first-order shear-deformation plate theory, the displacements in the Cartesian coordinate system can be expressed as follows:

$$u(x, y, z) = u_0(x, y) + z\theta_y(x, y), \quad (1)$$

$$v(x, y, z) = v_0(x, y) - z\theta_x(x, y), \quad (2)$$

$$w(x, y, z) = w_0(x, y), \quad (3)$$

where u_0 , v_0 , and w_0 are the displacements of the plate midplane in the x , y , and z directions and θ_x and θ_y denote the rotations with respect to x and y axes, respectively, as shown in Figure 1.

The relevant strain vector ε can be written in terms of the midplane deformations of equations (1)–(3), which gives

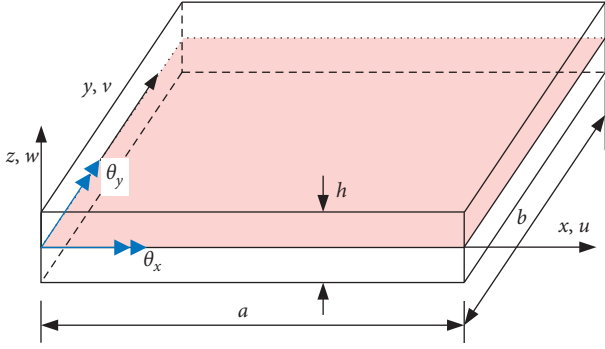


FIGURE 1: Positive directions of the deflection and two rotations.

$$\boldsymbol{\varepsilon} = \begin{Bmatrix} \varepsilon_{xx} \\ \varepsilon_{yy} \\ \gamma_{xy} \\ \gamma_{xz} \\ \gamma_{yz} \end{Bmatrix} = \begin{Bmatrix} \boldsymbol{\varepsilon}_m \\ \mathbf{0} \end{Bmatrix} + \begin{Bmatrix} \boldsymbol{\varepsilon}_b \\ \mathbf{0} \end{Bmatrix} + \begin{Bmatrix} \mathbf{0} \\ \boldsymbol{\varepsilon}_s \end{Bmatrix}, \quad (4)$$

where $\boldsymbol{\varepsilon}_m$, $\boldsymbol{\varepsilon}_b$, and $\boldsymbol{\varepsilon}_s$ are the membrane strain, the bending strain (curvature), and the shear strain, respectively:

$$\boldsymbol{\varepsilon}_m = \begin{Bmatrix} \frac{\partial u_0}{\partial x} \\ \frac{\partial v_0}{\partial y} \\ \frac{\partial u_0}{\partial y} + \frac{\partial v_0}{\partial x} \end{Bmatrix}, \quad (5)$$

$$\boldsymbol{\varepsilon}_b = z \begin{Bmatrix} \frac{\partial \theta_y}{\partial x} \\ \frac{\partial \theta_x}{\partial y} \\ \frac{\partial \theta_y}{\partial y} - \frac{\partial \theta_x}{\partial x} \end{Bmatrix},$$

$$\boldsymbol{\varepsilon}_s = \begin{Bmatrix} \frac{\partial w_0}{\partial x} + \theta_y \\ \frac{\partial w_0}{\partial y} - \theta_x \end{Bmatrix}.$$

By applying the principle of virtual work, the weak form can be stated as follows:

$$\int_{\Omega} \delta \boldsymbol{\varepsilon}_m^T \mathbf{D}_m \boldsymbol{\varepsilon}_m d\Omega + \int_{\Omega} \delta \boldsymbol{\varepsilon}_b^T \mathbf{D}_b \boldsymbol{\varepsilon}_b d\Omega + \int_{\Omega} \delta \boldsymbol{\varepsilon}_s^T \mathbf{D}_s \boldsymbol{\varepsilon}_s d\Omega - \int_{\Omega} \delta \mathbf{u}^T \tilde{\mathbf{f}} d\Omega - \int_{\Gamma} \delta \mathbf{u}^T \tilde{\mathbf{t}} d\Gamma = 0, \quad (6)$$

where \mathbf{D}_m is the membrane stiffness constitutive coefficients, \mathbf{D}_b represents the bending stiffness constitutive coefficients, and \mathbf{D}_s denotes the transverse shear stiffness constitutive coefficients defined as

$$\mathbf{D}_m = \int_{-t/2}^{t/2} \mathbf{D}_0 dz = t \mathbf{D}_0, \quad (7)$$

$$\mathbf{D}_b = \int_{-t/2}^{t/2} z^2 \mathbf{D}_0 dz = \frac{t^3}{12} \mathbf{D}_0, \quad (8)$$

$$\mathbf{D}_s = \int_{-t/2}^{t/2} \kappa G \begin{bmatrix} 1 & 0 \\ 0 & 1 \end{bmatrix} dz = \kappa t G \begin{bmatrix} 1 & 0 \\ 0 & 1 \end{bmatrix}, \quad (9)$$

in which G is the shear modulus, $\kappa = 5/6$ is the shear correction factor, and the matrix \mathbf{D}_0 contains the constitutive coefficients:

$$\mathbf{D}_0 = \frac{E}{1-\nu^2} \begin{bmatrix} 1 & \nu & 0 \\ \nu & 1 & 0 \\ 0 & 0 & \frac{(1-\nu)}{2} \end{bmatrix}, \quad (10)$$

where E and ν are Young's modulus and Poisson's ratio, respectively.

Based on the assumption of the first-order shear-deformation plate theory, the weak form for the free vibration analysis of the Reissner-Mindlin plate can be derived from the dynamic form of energy principle, i.e.,

$$\int_{\Omega} \delta \boldsymbol{\varepsilon}_m^T \mathbf{D}_m \boldsymbol{\varepsilon}_m d\Omega + \int_{\Omega} \delta \boldsymbol{\varepsilon}_b^T \mathbf{D}_b \boldsymbol{\varepsilon}_b d\Omega + \int_{\Omega} \delta \boldsymbol{\varepsilon}_s^T \mathbf{D}_s \boldsymbol{\varepsilon}_s d\Omega + \int_{\Omega} \delta \mathbf{d}^T \mathbf{m} \ddot{\mathbf{d}} d\Omega = 0, \quad (11)$$

where $\delta \mathbf{d}$ is the variation of the displacement field $\mathbf{d} = \{u_0 \ v_0 \ w_0 \ \theta_x \ \theta_y\}^T$ and \mathbf{m} is the inertia matrix containing the mass density ρ and thickness t :

$$\mathbf{m} = \rho \begin{bmatrix} t & 0 & 0 & 0 & 0 \\ 0 & t & 0 & 0 & 0 \\ 0 & 0 & t & 0 & 0 \\ 0 & 0 & 0 & \frac{t^3}{12} & 0 \\ 0 & 0 & 0 & 0 & \frac{t^3}{12} \end{bmatrix}. \quad (12)$$

For the buckling analysis, when the plate is subjected to in-plane prebuckling stresses σ_0 , the corresponding weak form can be reformulated as

$$\begin{aligned}
& \int_{\Omega} \delta \varepsilon_m^T \mathbf{D}_m \varepsilon_m d\Omega + \int_{\Omega} \delta \varepsilon_b^T \mathbf{D}_b \varepsilon_b d\Omega + \int_{\Omega} \delta \varepsilon_s^T \mathbf{D}_s \varepsilon_s d\Omega \\
& + t \int_{\Omega} \delta \nabla \mathbf{u}^T \begin{bmatrix} \sigma_0 & \mathbf{0} & \mathbf{0} \\ \mathbf{0} & \sigma_0 & \mathbf{0} \\ \mathbf{0} & \mathbf{0} & \sigma_0 \end{bmatrix} \nabla \mathbf{u} d\Omega + \frac{t^3}{12} \int_{\Omega} \delta \nabla \theta^T \begin{bmatrix} \sigma_0 & \mathbf{0} \\ \mathbf{0} & \sigma_0 \end{bmatrix} \nabla \theta d\Omega = 0,
\end{aligned} \tag{13}$$

where

$$\begin{aligned}
\sigma_0 &= \begin{bmatrix} \sigma_{xx}^0 & \tau_{xy}^0 \\ \tau_{xy}^0 & \sigma_{yy}^0 \end{bmatrix}, \\
\nabla \mathbf{u} &= \begin{bmatrix} \nabla u_0 \\ \nabla v_0 \\ \nabla w_0 \end{bmatrix}, \\
\nabla \theta &= \begin{bmatrix} \nabla \theta_x \\ \nabla \theta_y \end{bmatrix}, \\
\nabla &= \begin{bmatrix} \frac{\partial}{\partial x} \\ \frac{\partial}{\partial y} \end{bmatrix}.
\end{aligned} \tag{14}$$

Equation (13) can be rewritten in a compact form as

$$\begin{aligned}
& \int_{\Omega} \delta \varepsilon_m^T \mathbf{D}_m \varepsilon_m d\Omega + \int_{\Omega} \delta \varepsilon_b^T \mathbf{D}_b \varepsilon_b d\Omega + \int_{\Omega} \delta \varepsilon_s^T \mathbf{D}_s \varepsilon_s d\Omega \\
& + \int_{\Omega} \delta \varepsilon_g^T \boldsymbol{\tau} \varepsilon_g d\Omega = 0,
\end{aligned} \tag{15}$$

in which

$$\begin{aligned}
\boldsymbol{\tau} &= \begin{bmatrix} t\sigma_0 & \mathbf{0} & \mathbf{0} & \mathbf{0} & \mathbf{0} \\ \mathbf{0} & t\sigma_0 & \mathbf{0} & \mathbf{0} & \mathbf{0} \\ \mathbf{0} & \mathbf{0} & t\sigma_0 & \mathbf{0} & \mathbf{0} \\ \mathbf{0} & \mathbf{0} & \mathbf{0} & \frac{t^3\sigma_0}{12} & \mathbf{0} \\ \mathbf{0} & \mathbf{0} & \mathbf{0} & \mathbf{0} & \frac{t^3\sigma_0}{12} \end{bmatrix}, \\
\varepsilon_g^T &= \begin{bmatrix} u_{0,x} & u_{0,y} & 0 & 0 & 0 & 0 & 0 & 0 & 0 & 0 \\ 0 & 0 & v_{0,x} & v_{0,y} & 0 & 0 & 0 & 0 & 0 & 0 \\ 0 & 0 & 0 & 0 & w_{0,x} & w_{0,y} & 0 & 0 & 0 & 0 \\ 0 & 0 & 0 & 0 & 0 & 0 & \theta_{x,x} & \theta_{x,y} & 0 & 0 \\ 0 & 0 & 0 & 0 & 0 & 0 & 0 & 0 & \theta_{y,x} & \theta_{y,y} \end{bmatrix},
\end{aligned} \tag{16}$$

where “ $u_{0,x}$ ” represents the derivative of u_0 with respect to x .

2.2. Discrete Formulation for Reissner–Mindlin Plates. The bounded domain Ω is discretized into N_e triangular elements such that $\Omega = \cup_{e=1}^{N_e} \Omega^e$ and $\Omega^i \cap \Omega^j = \emptyset$, $i \neq j$. For any point in a 3-node triangular element, by using the nodal displacements at the nodes of the element using the shape functions, the generalized displacement field \mathbf{d} in the element is interpolated. The same shape functions are used for both displacements and rotations as

$$\mathbf{d} = \{u_0, v_0, w_0, \theta_x, \theta_y\}^T = \sum_{i=1}^{N_n} \mathbf{N}_i \mathbf{d}_i, \tag{17}$$

where N_n is the total number of nodes, $\mathbf{d}_i = \{u_{0i}, v_{0i}, w_{0i}, \theta_{xi}, \theta_{yi}\}^T$ is the generalized nodal displacement at node i , and $\mathbf{N}_i(\mathbf{x})$ is a diagonal matrix of shape functions given by

$$\mathbf{N}_i(\mathbf{x}) = \text{diag}\{N_i(\mathbf{x}), N_i(\mathbf{x}), N_i(\mathbf{x}), N_i(\mathbf{x}), N_i(\mathbf{x})\}. \tag{18}$$

Substituting equation (17) into (5), the membrane strain ε_m , the bending strain ε_b , and the shear strain ε_s can be written as

$$\varepsilon_m = \sum_{i=1}^{N_n} \mathbf{B}_{mi} \mathbf{d}_i, \tag{19}$$

$$\varepsilon_b = \sum_{i=1}^{N_n} \mathbf{B}_{bi} \mathbf{d}_i, \tag{20}$$

$$\varepsilon_s = \sum_{i=1}^{N_n} \mathbf{B}_{si} \mathbf{d}_i, \tag{21}$$

in which

$$\mathbf{B}_{mi} = \begin{bmatrix} N_{i,x} & 0 & 0 & 0 & 0 \\ 0 & N_{i,y} & 0 & 0 & 0 \\ N_{i,y} & N_{i,x} & 0 & 0 & 0 \end{bmatrix}, \tag{22}$$

$$\mathbf{B}_{bi} = \begin{bmatrix} 0 & 0 & 0 & 0 & N_{i,x} \\ 0 & 0 & 0 & -N_{i,y} & 0 \\ 0 & 0 & 0 & -N_{i,x} & N_{i,y} \end{bmatrix}, \tag{23}$$

$$\mathbf{B}_{si} = \begin{bmatrix} 0 & 0 & N_{i,x} & 0 & N_i \\ 0 & 0 & N_{i,y} & -N_i & 0 \end{bmatrix}, \tag{24}$$

where the subscript $i = 1, 2, 3$.

From equations (14)–(16), the geometrical strain ε_g can be written as

$$\varepsilon_g = \sum_{i=1}^{N_n} \mathbf{B}_{gi} \mathbf{d}_i, \tag{25}$$

in which

$$\mathbf{B}_{gi}^T = \begin{bmatrix} N_{i,x} & N_{i,y} & 0 & 0 & 0 & 0 & 0 & 0 & 0 & 0 \\ 0 & 0 & N_{i,x} & N_{i,y} & 0 & 0 & 0 & 0 & 0 & 0 \\ 0 & 0 & 0 & 0 & N_{i,x} & N_{i,y} & 0 & 0 & 0 & 0 \\ 0 & 0 & 0 & 0 & 0 & 0 & N_{i,x} & N_{i,y} & 0 & 0 \\ 0 & 0 & 0 & 0 & 0 & 0 & 0 & 0 & N_{i,x} & N_{i,y} \end{bmatrix}. \quad (26)$$

Substituting equations (22)–(24) into (6), a set of discretized algebraic system equations of Reissner–Mindlin plates for static analysis can be obtained in the following matrix form:

$$\mathbf{K}\hat{\mathbf{d}} - \hat{\mathbf{f}} = \mathbf{0}, \quad (27)$$

where $\hat{\mathbf{d}}$ denotes the vector of global nodal displacement at all of the nodes and $\hat{\mathbf{f}}$ is the force vector (including forces and torques) defined as

$$\hat{\mathbf{f}} = \int_{\Omega} \mathbf{N}(\mathbf{x})\mathbf{f} \, d\Omega + \int_{\Gamma} \mathbf{N}(\mathbf{x})\mathbf{t} \, d\Gamma, \quad (28)$$

where \mathbf{f} and \mathbf{t} denote the distributed load and prescribed boundary load, respectively.

In equation (27), the global stiffness matrix \mathbf{K} can be expressed as

$$\mathbf{K} = \sum_{e=1}^{N_e} (\mathbf{K}_m^{(e)} + \mathbf{K}_b^{(e)} + \mathbf{K}_s^{(e)}), \quad (29)$$

in which

$$\mathbf{K}_m^{(e)} = \int_{\Omega_e} \mathbf{B}_m^T \mathbf{D}_m \mathbf{B}_m \, d\Omega, \quad (30)$$

$$\mathbf{K}_b^{(e)} = \int_{\Omega_e} \mathbf{B}_b^T \mathbf{D}_b \mathbf{B}_b \, d\Omega, \quad (31)$$

$$\mathbf{K}_s^{(e)} = \int_{\Omega_e} \mathbf{B}_s^T \mathbf{D}_s \mathbf{B}_s \, d\Omega. \quad (32)$$

For free vibration, we have

$$(\mathbf{K} - \omega^2 \mathbf{M})\hat{\mathbf{d}} = \mathbf{0}, \quad (33)$$

where ω denotes the natural frequency and \mathbf{M} is the global inertia matrix:

$$\mathbf{M} = \sum_{k=1}^{N_e} \int_{\Omega_e} \mathbf{N}^T \mathbf{m} \mathbf{N} \, d\Omega. \quad (34)$$

For the buckling analysis, we have

$$(\mathbf{K} - \lambda_{cr} \mathbf{K}_g)\hat{\mathbf{d}} = \mathbf{0}, \quad (35)$$

where

$$\mathbf{K}_g = \sum_{k=1}^{N_e} \int_{\Omega_e} \mathbf{B}_g^T \boldsymbol{\tau} \mathbf{B}_g \, d\Omega, \quad (36)$$

which is the geometrical stiffness matrix, and λ_{cr} denotes the critical buckling load. In addition, it is noted that the

summation in equations (29), (34), and (36) means an assembly process.

3. The Formulation of Gradient Stable Node-Based Smoothed Integration and Discrete Shear Gap Technique

According to the introduction in Section 2.2, the structural stiffness matrix is composed of three parts, namely, \mathbf{K}_m , \mathbf{K}_b , and \mathbf{K}_s . On the one hand, for \mathbf{K}_m and \mathbf{K}_b , we take the method of gradient stable node-based smoothed integration to avoid temporal instability and spatial instability; for \mathbf{K}_s , on the other hand, the discrete shear gap technique is employed to avoid the shear-locking problem. The formula for the smoothed integral is derived from the Hu–Washizu three-field variational principle as shown in Section 3.1, and its discrete form is given in Section 3.2. The discrete shear technology is introduced in Section 3.3.

3.1. Gradient Stable Smoothed Derivative Correction. Based on the Hu–Washizu three-field variational principle, Duan [68] gives the corrected nodal derivative using more rigorous mathematics, and the quadratically consistent nodal integration is proposed for second-order meshfree Galerkin methods. However, the proposal is more complex and requires two-order Gauss integration of the boundary integral. In this paper, a simplified scheme is provided by using another correct method.

Assume that \mathbf{u} and $\boldsymbol{\sigma}$ are the displacement and assumed Cauchy stress, respectively, $\tilde{\boldsymbol{\varepsilon}}$ is the interpolated strain or smoothed strain, and $\boldsymbol{\varepsilon}$ is the actual strain. The Hu–Washizu three-field weak form for the elastic-static problem can be written as

$$\begin{aligned} \delta\Pi^*(\mathbf{u}, \tilde{\boldsymbol{\varepsilon}}, \boldsymbol{\sigma}) = & \int_{\Omega} \delta\tilde{\boldsymbol{\varepsilon}}^T \mathbf{D} \tilde{\boldsymbol{\varepsilon}} \, d\Omega - \int_{\Gamma_t} \delta\mathbf{u}^T \mathbf{t} \, d\Gamma - \int_{\Omega} \delta\mathbf{u}^T \mathbf{f} \, d\Omega \\ & + \delta \int_{\Omega} \hat{\boldsymbol{\sigma}}^T (\boldsymbol{\varepsilon} - \tilde{\boldsymbol{\varepsilon}}) \, d\Omega. \end{aligned} \quad (37)$$

Clearly, if the interpolated strain $\tilde{\boldsymbol{\varepsilon}}$ can be somehow constructed from the displacement \mathbf{u} and meet the following orthogonality condition:

$$\int_{\Omega} \hat{\boldsymbol{\sigma}}^T (\boldsymbol{\varepsilon} - \tilde{\boldsymbol{\varepsilon}}) \, d\Omega = 0. \quad (38)$$

Then, a form containing only independent variables can be obtained as simple as the classical one:

$$\delta\Pi^{**}(\mathbf{u}, \tilde{\boldsymbol{\varepsilon}}, \boldsymbol{\sigma}) = \int_{\Omega} \delta\tilde{\boldsymbol{\varepsilon}}^T \mathbf{D} \tilde{\boldsymbol{\varepsilon}} \, d\Omega - \int_{\Gamma_t} \delta\mathbf{u}^T \bar{\mathbf{t}} \, d\Gamma - \int_{\Omega} \delta\mathbf{u}^T \bar{\mathbf{f}} \, d\Omega. \quad (39)$$

Deriving by reference [68], in order to meet the orthogonality condition as equation (38), let the following equation be satisfied for each subdomain Ω_L and expressed as a finite element form:

$$\int_{\Omega_L} \hat{\boldsymbol{\sigma}}^T \left(\frac{\partial N_I}{\partial x_i} - \frac{\partial \tilde{N}_I}{\partial x_i} \right) d\Omega = 0, \quad (40)$$

where N_I is the shape function corresponding to strain ε in element I and \tilde{N}_I is the shape function corresponding to smoothed strain $\tilde{\varepsilon}$ in element I . Since stress and strain are related to the first partial derivative of displacement, which is a polynomial combination of coordinates, stress can also be regarded as a polynomial of position. Equation (40) can be equivalent to the following:

$$\int_{\Omega_L} \mathbf{q}(\mathbf{x}) \left(\frac{\partial N_I}{\partial x_i} - \frac{\partial \tilde{N}_I}{\partial x_i} \right) d\Omega = 0, \quad (41)$$

where $\mathbf{q}(\mathbf{x})$ is the space base which is one order lower than the space for the displacement \mathbf{u} .

Different from reference [68] which chose the quadratic base for displacement, the first base is selected for displacement as the shape function of the first-order triangular element, and $\mathbf{q}(\mathbf{x}) = 1$. Then, the following equations can be obtained:

$$\int_{\Omega_L} \frac{\partial \tilde{N}_I}{\partial x_i} d\Omega = \int_{\Gamma_L} N_I n_i d\Gamma, \quad (42)$$

$$\int_{\Omega_L} \frac{\partial \tilde{N}_I^2}{\partial x_i \partial x_j} d\Omega = \int_{\Gamma_L} N_I n_j d\Gamma. \quad (43)$$

In the nodal integration scheme, node L is the only point in Ω_L , and there exists only one unknown $\tilde{N}_{I,x}(\mathbf{x}_L)$. Hence, equations (42) and (43) cannot be satisfied at the same time. To this end, we introduce the derivatives of the function $\tilde{N}_{I,x}$ by means of Taylor's expansion such that $\tilde{N}_{I,xx}(\mathbf{x}_L)$ and $\tilde{N}_{I,xy}(\mathbf{x}_L)$ are introduced and can serve as the other two unknowns. Taylor's expansion for $\tilde{N}_{I,x}$ can be formulated as

$$\begin{aligned} \tilde{N}_{I,x}(\mathbf{x}) &= \tilde{N}_{I,x}(\mathbf{x}_L) + (x - x_L) \tilde{N}_{I,xx}(\mathbf{x}_L) \\ &\quad + (y - y_L) \tilde{N}_{I,xy}(\mathbf{x}_L) + \text{H.O.T}, \end{aligned} \quad (44)$$

$$\tilde{N}_{I,xx}(\mathbf{x}) = \tilde{N}_{I,xx}(\mathbf{x}_L) + \text{H.O.T}, \quad (45)$$

$$\tilde{N}_{I,xy}(\mathbf{x}) = \tilde{N}_{I,xy}(\mathbf{x}_L) + \text{H.O.T}, \quad (46)$$

where H.O.T means higher-order terms.

Substitution of equations (56)–(58) into (42) and (43) leads to

$$\begin{bmatrix} A_L & I_L^x & I_L^y \\ 0 & A_L & 0 \\ 0 & 0 & A_L \end{bmatrix} \begin{Bmatrix} \tilde{N}_{I,x}(\mathbf{x}_L) \\ \tilde{N}_{I,xx}(\mathbf{x}_L) \\ \tilde{N}_{I,xy}(\mathbf{x}_L) \end{Bmatrix} = \begin{Bmatrix} \int_{\Gamma_L} N_I n_x d\Gamma \\ \int_{\Gamma_L} N_{I,x} n_x d\Gamma \\ \int_{\Gamma_L} N_{I,x} n_y d\Gamma \end{Bmatrix}, \quad (47)$$

where $A_L = \int_{\Omega_L} d\Omega$ is the area of Ω_L and

$$I_L^x = \int_{\Omega_L} (x - x_L) d\Omega, \quad (48)$$

$$I_L^y = \int_{\Omega_L} (y - y_L) d\Omega.$$

By solving equation (47), the corrected nodal derivative $\tilde{N}_{I,x}(\mathbf{x}_L)$ and its derivatives, i.e., $\tilde{N}_{I,xx}(\mathbf{x}_L)$ and $\tilde{N}_{I,xy}(\mathbf{x}_L)$, are obtained. Following the same derivation, Taylor's expansion for $\tilde{N}_{I,y}$ is

$$\begin{aligned} \tilde{N}_{I,y}(\mathbf{x}) &= \tilde{N}_{I,y}(\mathbf{x}_L) + (x - x_L) \tilde{N}_{I,yx}(\mathbf{x}_L) \\ &\quad + (y - y_L) \tilde{N}_{I,yy}(\mathbf{x}_L) + \text{H.O.T}, \end{aligned} \quad (49)$$

$$\tilde{N}_{I,yx}(\mathbf{x}) = \tilde{N}_{I,yx}(\mathbf{x}_L) + \text{H.O.T}, \quad (50)$$

$$\tilde{N}_{I,yy}(\mathbf{x}) = \tilde{N}_{I,yy}(\mathbf{x}_L) + \text{H.O.T}. \quad (51)$$

The equation for y -derivatives can be written as

$$\begin{bmatrix} A_L & I_L^x & I_L^y \\ 0 & A_L & 0 \\ 0 & 0 & A_L \end{bmatrix} \begin{Bmatrix} \tilde{N}_{I,y}(\mathbf{x}_L) \\ \tilde{N}_{I,yx}(\mathbf{x}_L) \\ \tilde{N}_{I,yy}(\mathbf{x}_L) \end{Bmatrix} = \begin{Bmatrix} \int_{\Gamma_L} N_I n_y d\Gamma \\ \int_{\Gamma_L} N_{I,y} n_x d\Gamma \\ \int_{\Gamma_L} N_{I,y} n_y d\Gamma \end{Bmatrix}. \quad (52)$$

To simplify the calculation, the equivalent circle domain can be assumed for the subdomain Ω_L . The area A_L , first moments I_{Lx} and I_{Ly} , and second moments of inertia I_{Lxx} , I_{Lxy} , and I_{Lyy} of each nodal domain can be expressed as

$$A_L = \int_{\Omega_L} d\Omega,$$

$$I_{Lx} = I_{Ly} = I_{Lxy} = 0, \quad (53)$$

$$I_{Lxx} = I_{Lyy} = \frac{A_L^2}{4\pi}.$$

It should be noted that the concept of equivalent circles is only introduced to simplify the calculation of these integrals, and the actual smooth region is still a polygon composed of elements and nodes.

3.2. Discrete Form of Gradient Stabilized Nodal Integration.

In this part, the nodal integration formulation will be introduced. We can discretize the problem domain Ω with N_e triangular elements as in standard FEM, but the integral required in this work is now based on the node and utilizes strain smoothing operations. In the process of such node integration, the middle edge points are connected with the center points of the surrounding triangular elements in order to form the smoothed domain of each node sequentially, as shown in Figure 2, such that $\Omega = \cup_{k=1}^{N_n} \Omega_k$ and $\Omega_i \cap \Omega_j = \phi$ for $i \neq j$, in which N_n is the total number of nodes of the problem domain.

From equations (44)–(46) and equations (49)–(51), the smoothed strain $\tilde{\varepsilon}_m(\mathbf{x})$ and $\tilde{\varepsilon}_b(\mathbf{x})$ in Ω_L surrounding node L can be expressed as

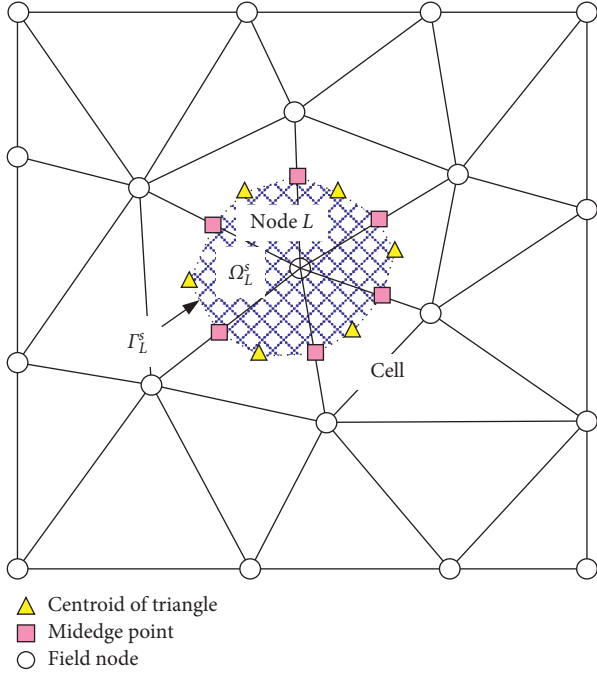


FIGURE 2: Triangular elements and smoothing cells associated with nodes.

$$\tilde{\varepsilon}_m(\mathbf{x}) = \tilde{\varepsilon}_m^{(L)} + \tilde{\varepsilon}_{mx}^{(L)}(x - x_L) + \tilde{\varepsilon}_{my}^{(L)}(y - y_L), \quad (54)$$

$$\tilde{\varepsilon}_b(\mathbf{x}) = \tilde{\varepsilon}_b^{(L)} + \tilde{\varepsilon}_{bx}^{(L)}(x - x_L) + \tilde{\varepsilon}_{by}^{(L)}(y - y_L), \quad (55)$$

where

$$\begin{aligned} \tilde{\varepsilon}_m^{(L)} &= \tilde{\mathbf{B}}_m^{(L)} \hat{\mathbf{d}}, \\ \tilde{\varepsilon}_{mx}^{(L)} &= \tilde{\mathbf{B}}_{mx}^{(L)} \hat{\mathbf{d}}, \\ \tilde{\varepsilon}_{my}^{(L)} &= \tilde{\mathbf{B}}_{my}^{(L)} \hat{\mathbf{d}}, \end{aligned} \quad (56)$$

$$\begin{aligned} \tilde{\varepsilon}_b^{(L)} &= \tilde{\mathbf{B}}_b^{(L)} \hat{\mathbf{d}}, \\ \tilde{\varepsilon}_{bx}^{(L)} &= \tilde{\mathbf{B}}_{bx}^{(L)} \hat{\mathbf{d}}, \\ \tilde{\varepsilon}_{by}^{(L)} &= \tilde{\mathbf{B}}_{by}^{(L)} \hat{\mathbf{d}}, \end{aligned} \quad (57)$$

in which

$$\begin{aligned} \tilde{\mathbf{B}}_m^{(L)} &= \left[\tilde{\mathbf{B}}_{m1}^{(L)} \cdots \tilde{\mathbf{B}}_{mI}^{(L)} \cdots \tilde{\mathbf{B}}_{mN_n}^{(L)} \right], \\ \tilde{\mathbf{B}}_b^{(L)} &= \left[\tilde{\mathbf{B}}_{b1}^{(L)} \cdots \tilde{\mathbf{B}}_{bI}^{(L)} \cdots \tilde{\mathbf{B}}_{bN_n}^{(L)} \right], \end{aligned} \quad (58)$$

$$\begin{aligned} \tilde{\mathbf{B}}_{mx}^{(L)} &= \left[\tilde{\mathbf{B}}_{mx1}^{(L)} \cdots \tilde{\mathbf{B}}_{mxI}^{(L)} \cdots \tilde{\mathbf{B}}_{mxN_n}^{(L)} \right], \\ \tilde{\mathbf{B}}_{bx}^{(L)} &= \left[\tilde{\mathbf{B}}_{bx1}^{(L)} \cdots \tilde{\mathbf{B}}_{bxI}^{(L)} \cdots \tilde{\mathbf{B}}_{bxN_n}^{(L)} \right], \end{aligned} \quad (59)$$

$$\begin{aligned} \tilde{\mathbf{B}}_{my}^{(L)} &= \left[\tilde{\mathbf{B}}_{my1}^{(L)} \cdots \tilde{\mathbf{B}}_{myI}^{(L)} \cdots \tilde{\mathbf{B}}_{myN_n}^{(L)} \right], \\ \tilde{\mathbf{B}}_{by}^{(L)} &= \left[\tilde{\mathbf{B}}_{by1}^{(L)} \cdots \tilde{\mathbf{B}}_{byI}^{(L)} \cdots \tilde{\mathbf{B}}_{byN_n}^{(L)} \right], \end{aligned} \quad (60)$$

$$\tilde{\mathbf{B}}_{mI}^{(L)} = \begin{bmatrix} \tilde{N}_{I,x} & 0 & 0 & 0 & 0 \\ 0 & \tilde{N}_{I,y} & 0 & 0 & 0 \\ \tilde{N}_{I,y} & \tilde{N}_{I,x} & 0 & 0 & 0 \end{bmatrix}, \quad (61)$$

$$\tilde{\mathbf{B}}_{bI}^{(L)} = \begin{bmatrix} 0 & 0 & 0 & 0 & \tilde{N}_{I,x} \\ 0 & 0 & 0 & -\tilde{N}_{I,y} & 0 \\ 0 & 0 & 0 & -\tilde{N}_{I,x} & \tilde{N}_{I,y} \end{bmatrix},$$

$$\tilde{\mathbf{B}}_{mxI}^{(L)} = \begin{bmatrix} \tilde{N}_{I,xx} & 0 & 0 & 0 & 0 \\ 0 & \tilde{N}_{I,yx} & 0 & 0 & 0 \\ \tilde{N}_{I,yx} & \tilde{N}_{I,xx} & 0 & 0 & 0 \end{bmatrix}, \quad (62)$$

$$\tilde{\mathbf{B}}_{bxI}^{(L)} = \begin{bmatrix} 0 & 0 & 0 & 0 & \tilde{N}_{I,xx} \\ 0 & 0 & 0 & -\tilde{N}_{I,yx} & 0 \\ 0 & 0 & 0 & -\tilde{N}_{I,xx} & \tilde{N}_{I,yx} \end{bmatrix},$$

$$\tilde{\mathbf{B}}_{myI}^{(L)} = \begin{bmatrix} \tilde{N}_{I,xy} & 0 & 0 & 0 & 0 \\ 0 & \tilde{N}_{I,yy} & 0 & 0 & 0 \\ \tilde{N}_{I,yy} & \tilde{N}_{I,xy} & 0 & 0 & 0 \end{bmatrix}, \quad (63)$$

$$\tilde{\mathbf{B}}_{byI}^{(L)} = \begin{bmatrix} 0 & 0 & 0 & 0 & \tilde{N}_{I,xy} \\ 0 & 0 & 0 & -\tilde{N}_{I,yy} & 0 \\ 0 & 0 & 0 & -\tilde{N}_{I,xy} & \tilde{N}_{I,yy} \end{bmatrix}.$$

3.3. Formulation of the Stabilized Discrete Shear Gap Technique. The discrete shear gap method is adopted here to eliminate the shear locking. In each triangular element, the nodes are denoted anticlockwise as i , j , and k , respectively. The shear strain can be given as

$$\gamma_{xz} = \sum_m N_{m,x}(\mathbf{x}) \Delta w_{xm} + \sum_m N_{m,x}(\mathbf{x}) \Delta w_{ym}, \quad (64)$$

$$\gamma_{yz} = \sum_m N_{m,y}(\mathbf{x}) \Delta w_{xm} + \sum_m N_{m,y}(\mathbf{x}) \Delta w_{ym}, \quad (65)$$

where Δw_{xm} and Δw_{ym} are the discrete shear gaps at the node m given by

$$\Delta w_{xi} = \Delta w_{xk} = \Delta w_{yi} = \Delta w_{yj} = 0, \quad (66)$$

$$\Delta w_{xj} = (w_j - w_i) - \frac{1}{2}b(\theta_{xi} + \theta_{xj}) + \frac{1}{2}a(\theta_{yi} + \theta_{yj}), \quad (67)$$

$$\Delta w_{yk} = (w_k - w_i) - \frac{1}{2}d(\theta_{xi} + \theta_{xk}) + \frac{1}{2}c(\theta_{yi} + \theta_{yk}), \quad (68)$$

where

$$a = x_j - x_i, \quad (69)$$

$$b = y_j - y_i,$$

$$c = x_k - x_i, \quad (70)$$

$$d = y_k - y_i.$$

From equations (64)–(70), the shear strain ε_s in each element can be rewritten as

$$\varepsilon_s = \begin{Bmatrix} \gamma_{xz} \\ \gamma_{yz} \end{Bmatrix} = \mathbf{B}_s \mathbf{d} = [\mathbf{B}_{si} \ \mathbf{B}_{sj} \ \mathbf{B}_{sk}] \begin{Bmatrix} \mathbf{d}_i \\ \mathbf{d}_j \\ \mathbf{d}_k \end{Bmatrix}, \quad (71)$$

in which

$$\mathbf{B}_{si} = \frac{1}{2A_e} \begin{bmatrix} 0 & 0 & b-d & 0 & A_e \\ 0 & 0 & c-a & -A_e & 0 \end{bmatrix}, \quad (72)$$

$$\mathbf{B}_{sj} = \frac{1}{2A_e} \begin{bmatrix} 0 & 0 & d & -\frac{bd}{2} & \frac{ad}{2} \\ 0 & 0 & -c & \frac{bc}{2} & -\frac{ac}{2} \end{bmatrix}, \quad (73)$$

$$\mathbf{B}_{sk} = \frac{1}{2A_e} \begin{bmatrix} 0 & 0 & -b & \frac{bd}{2} & -\frac{bc}{2} \\ 0 & 0 & a & -\frac{ad}{2} & \frac{ac}{2} \end{bmatrix}, \quad (74)$$

where A_e is the area of the element.

To improve significantly the accuracy of approximate solutions and to stabilize shear force oscillations presenting the triangular element, a stabilization technique [69, 70] needs to be added to the original discrete shear gap element. Therefore, the transverse shear stiffness constitutive coefficients \mathbf{D}_s should be corrective as $\bar{\mathbf{D}}_s$:

$$\bar{\mathbf{D}}_s = \frac{\kappa t^3 G}{t^2 + \alpha h_e^2} \begin{bmatrix} 1 & 0 \\ 0 & 1 \end{bmatrix}, \quad (75)$$

where α is a positive constant [69, 71] and the characteristic length h_e can be estimated as the diameter of the equation circle domain:

$$h_e = 2\sqrt{\frac{A_e}{\pi}}. \quad (76)$$

3.4. Discrete Formulation for GS-DSG Method. We now seek for a weak form solution of the generalized displacement field \mathbf{d} that satisfies the following smoothed Galerkin weak form:

$$\int_{\Omega} \delta \bar{\varepsilon}_m^T \mathbf{D}_m \bar{\varepsilon}_m \, d\Omega + \int_{\Omega} \delta \bar{\varepsilon}_b^T \mathbf{D}_b \bar{\varepsilon}_b \, d\Omega + \int_{\Omega} \varepsilon_s^T \mathbf{D}_s \varepsilon_s \, d\Omega - \int_{\Omega} \delta \mathbf{d}^T \mathbf{f} \, d\Omega - \int_{\Gamma} \delta \mathbf{d}^T \mathbf{t} \, d\Gamma = 0. \quad (77)$$

Substituting equations (74)–(76) into (77), a set of discretized algebraic system equations can be obtained in the following matrix form:

$$\tilde{\mathbf{K}} \hat{\mathbf{d}} - \hat{\mathbf{f}} = \mathbf{0}, \quad (78)$$

where $\tilde{\mathbf{K}}$ is the global smoothed stiffness matrix assembled in the form of

$$\tilde{\mathbf{K}} = \sum_{L=1}^{N_n} \left(\tilde{\mathbf{K}}_m^{(L)} + \tilde{\mathbf{K}}_b^{(L)} \right) + \sum_{e=1}^{N_e} \mathbf{K}_s^{(e)}. \quad (79)$$

The summation in equation (79) means an assembly process same as the practice in the FEM, and N_n is the number of the nodes of the whole problem domain Ω . $\mathbf{K}_s^{(e)}$ is given from equation (32) by using the stabilized discrete shear gap method to eliminate the shear locking. $\tilde{\mathbf{K}}_m^{(L)}$ and $\tilde{\mathbf{K}}_b^{(L)}$ are the stiffness matrices associated with node L given as

$$\tilde{\mathbf{K}}_m^{(L)} = \left(\tilde{\mathbf{B}}_m^{(L)} \right)^T \mathbf{D}_m \left(\tilde{\mathbf{B}}_m^{(L)} \right) A_L + \left(\tilde{\mathbf{B}}_{mx}^{(L)} \right)^T \mathbf{D}_m \left(\tilde{\mathbf{B}}_{mx}^{(L)} \right) I_{Lxx} + \left(\tilde{\mathbf{B}}_{my}^{(L)} \right)^T \mathbf{D}_m \left(\tilde{\mathbf{B}}_{my}^{(L)} \right) I_{Lyy}, \quad (80)$$

$$\tilde{\mathbf{K}}_b^{(L)} = \left(\tilde{\mathbf{B}}_b^{(L)} \right)^T \mathbf{D}_b \left(\tilde{\mathbf{B}}_b^{(L)} \right) A_L + \left(\tilde{\mathbf{B}}_{bx}^{(L)} \right)^T \mathbf{D}_b \left(\tilde{\mathbf{B}}_{bx}^{(L)} \right) I_{Lxx} + \left(\tilde{\mathbf{B}}_{by}^{(L)} \right)^T \mathbf{D}_b \left(\tilde{\mathbf{B}}_{by}^{(L)} \right) I_{Lyy}. \quad (81)$$

For free vibration, we have

$$\left(\tilde{\mathbf{K}} - \omega^2 \mathbf{M} \right) \hat{\mathbf{d}} = \mathbf{0}. \quad (82)$$

For the buckling analysis, we have

$$\left(\tilde{\mathbf{K}} - \lambda_{cr} \tilde{\mathbf{K}}_g \right) \hat{\mathbf{d}} = \mathbf{0}, \quad (83)$$

where $\tilde{\mathbf{K}}_g$ denotes the geometrical stiffness matrix assembled in the form of

$$\tilde{\mathbf{K}}_g = \sum_{L=1}^{N_n} \tilde{\mathbf{K}}_g^{(L)}. \quad (84)$$

The nodal geometrical stiffness matrix $\tilde{\mathbf{K}}_g^{(L)}$ in equation (84) can be calculated by

$$\begin{aligned} \tilde{\mathbf{K}}_g^{(L)} = & \left(\tilde{\mathbf{B}}_g^{(L)} \right)^T \boldsymbol{\tau} \left(\tilde{\mathbf{B}}_g^{(L)} \right) A_L + \left(\tilde{\mathbf{B}}_{gx}^{(L)} \right)^T \boldsymbol{\tau} \left(\tilde{\mathbf{B}}_{gx}^{(L)} \right) I_{Lxx} \\ & + \left(\tilde{\mathbf{B}}_{gy}^{(L)} \right)^T \boldsymbol{\tau} \left(\tilde{\mathbf{B}}_{gy}^{(L)} \right) I_{Lyy}, \end{aligned} \quad (85)$$

with

$$\left(\tilde{\mathbf{B}}_g^{(L)} \right)^T = \begin{bmatrix} \tilde{N}_{i,x} & \tilde{N}_{i,y} & 0 & 0 & 0 & 0 & 0 & 0 & 0 & 0 \\ 0 & 0 & \tilde{N}_{i,x} & \tilde{N}_{i,y} & 0 & 0 & 0 & 0 & 0 & 0 \\ 0 & 0 & 0 & 0 & \tilde{N}_{i,x} & \tilde{N}_{i,y} & 0 & 0 & 0 & 0 \\ 0 & 0 & 0 & 0 & 0 & 0 & \tilde{N}_{i,x} & \tilde{N}_{i,y} & 0 & 0 \\ 0 & 0 & 0 & 0 & 0 & 0 & 0 & 0 & \tilde{N}_{i,x} & \tilde{N}_{i,y} \end{bmatrix}, \quad (86)$$

$$\left(\tilde{\mathbf{B}}_{gx}^{(L)} \right)^T = \begin{bmatrix} \tilde{N}_{i,xx} & \tilde{N}_{i,yx} & 0 & 0 & 0 & 0 & 0 & 0 & 0 & 0 \\ 0 & 0 & \tilde{N}_{i,xx} & \tilde{N}_{i,yx} & 0 & 0 & 0 & 0 & 0 & 0 \\ 0 & 0 & 0 & 0 & \tilde{N}_{i,xx} & \tilde{N}_{i,yx} & 0 & 0 & 0 & 0 \\ 0 & 0 & 0 & 0 & 0 & 0 & \tilde{N}_{i,xx} & \tilde{N}_{i,yx} & 0 & 0 \\ 0 & 0 & 0 & 0 & 0 & 0 & 0 & 0 & \tilde{N}_{i,xx} & \tilde{N}_{i,yx} \end{bmatrix}, \quad (87)$$

$$\left(\tilde{\mathbf{B}}_{gy}^{(L)} \right)^T = \begin{bmatrix} \tilde{N}_{i,xy} & \tilde{N}_{i,yy} & 0 & 0 & 0 & 0 & 0 & 0 & 0 & 0 \\ 0 & 0 & \tilde{N}_{i,xy} & \tilde{N}_{i,yy} & 0 & 0 & 0 & 0 & 0 & 0 \\ 0 & 0 & 0 & 0 & \tilde{N}_{i,xy} & \tilde{N}_{i,yy} & 0 & 0 & 0 & 0 \\ 0 & 0 & 0 & 0 & 0 & 0 & \tilde{N}_{i,xy} & \tilde{N}_{i,yy} & 0 & 0 \\ 0 & 0 & 0 & 0 & 0 & 0 & 0 & 0 & \tilde{N}_{i,xy} & \tilde{N}_{i,yy} \end{bmatrix}. \quad (88)$$

4. Numerical Examples

In this section, static, free vibration, and buckling analyses of square, T-shape, elliptical, and rectangular plates are considered. In addition, the present method is compared with other three methods, the FEM-DSG, NS-FEM, and NS-DSG methods. To examine the numerical error precisely, the displacement error norm is defined as

$$e_u = \sqrt{\frac{\sum_{i=1}^{N_n} (u_i^{\text{exact}} - u_i^{\text{num}})^2}{\sum_{i=1}^{N_n} (u_i^{\text{exact}})^2}}, \quad (89)$$

where the superscript “exact” denotes the exact solution (if an exact solution does not exist, “exact” is the reference solution) and “num” represents the displacement vector obtained using numerical methods including the present method.

In the following example, material parameters’ Young’s modulus is expressed as E , Poisson’s ratio is expressed as ν , and mass density is expressed as ρ .

4.1. Static Analysis

4.1.1. Square Plate. Consider the model of a simply supported square plate subjected to a uniform load $q = 1$ as shown in

Figure 3. The geometric and material parameters are length $L = 10$ and thickness $t = 2.0$; $E = 2.1 \times 10^9$ and $\nu = 0.3$. Due to symmetry, only a quarter of the plate is modeled to reduce the computation cost, and uniform meshes are employed. The center deflection w_c is normalized as $\hat{w} = w_c D / q L^4$, where $D = Et^3 / (12(1 - \nu^2))$ is the bending stiffness. In order to test the performance of the mentioned numerical methods, the numerical results obtained using the present method are compared with other three methods. The result calculated by the ABAQUS software is used for reference, using S4R elements and a large number (37,249) of nodes.

Table 1 shows the numerical results of the normalized center deflection. Figure 4 shows the relative error, and the label “mesh density” on the horizontal axis shows the number of cells on each side. Figure 5 shows the convergence status of the displacement error norm e_u , where h is the average nodal spacing of the node distribution. From the results, it can be seen that the deflection obtained by NS-FEM and NS-DSG is larger than the reference solution, whereas the deflection solved by the proposed method and FEM-DSG is smaller than the reference solution. Meanwhile, the proposed method is more accurate than the others. By comparing the convergence rate of the methods as shown in Figure 5, the proposed method has a higher convergence rate than the others, as far as the average nodal spacing trail off is concerned.

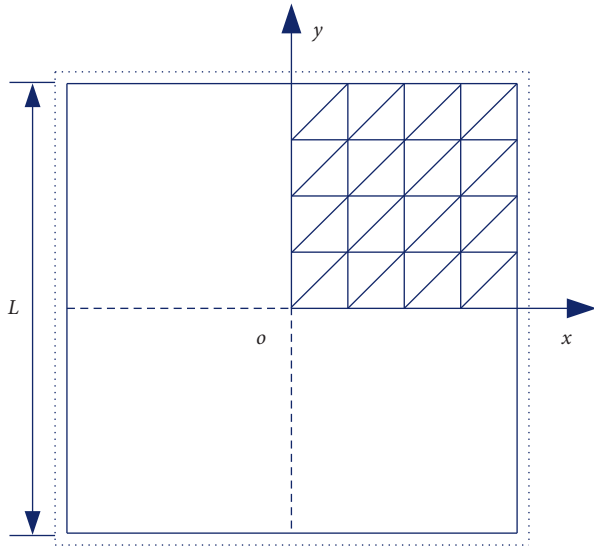


FIGURE 3: A square plate with a simply supported boundary condition.

TABLE 1: Numerical results of normalized central deflection \hat{w} for the simply supported square plate subjected to uniform load.

Mesh	FEM-DSG	NS-FEM	NS-DSG	GS-DSG
8×8	0.005442	0.005678	0.005567	0.005519
16×16	0.005516	0.005585	0.005554	0.005540
24×24	0.005532	0.005563	0.005550	0.005544
32×32	0.005538	0.005555	0.005549	0.005545
Reference	0.005545			

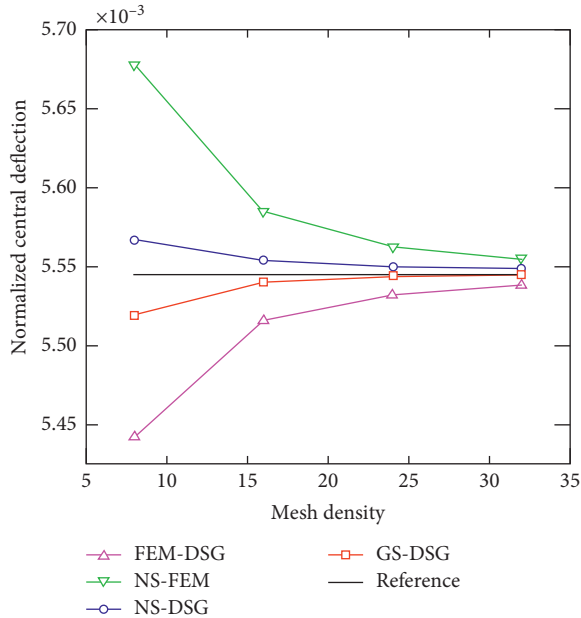


FIGURE 4: Central deflection.

4.1.2. T-Shaped Plate. In this section, a T-shaped plate with clamped edges and subjected to two kinds of loads, i.e., uniform and concentrated loads, is analyzed to further

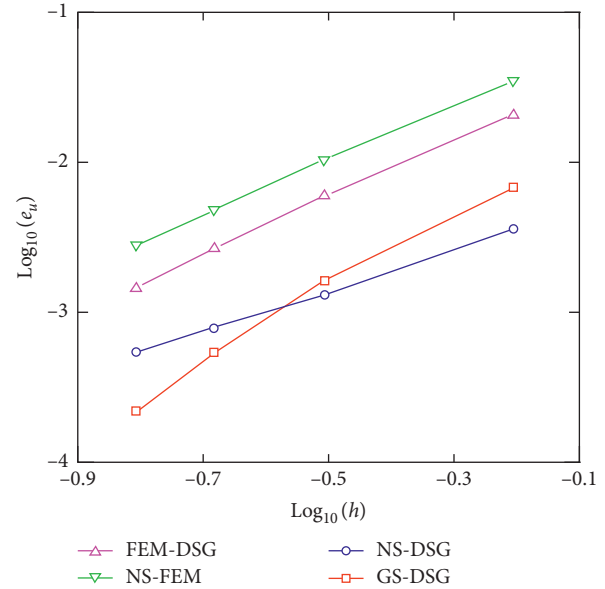


FIGURE 5: Convergence properties.

examine the efficiency of the present method. The geometric parameters are shown in Figure 6. Two thickness are considered, $t = 0.01$ and $t = 0.5$. Material parameters are $E = 2.1 \times 10^9$ and $\nu = 0.3$. The uniform load applied to the entire plate is given by $q = 0.01$, and the concentrated load applied to point A is taken as $p = 1$. Due to the symmetry of the plate, only half of the model is studied to reduce the calculation cost.

Figure 7 shows the mesh model, which is discretized using 154 nodes with 243 triangular elements. Numerical results of the present method are compared with other three methods. Since the analytical solution is unavailable for this problem, the result calculated by the ABAQUS software with a very fine mesh (2751 nodes and 5200 elements) was used for reference. The deflections along the line OA are plotted as shown in Figures 8 and 9. From the results, it can be seen that, for the thick plate, the results are almost identical, and the result is close to the reference solution. That is, because the shear-locking phenomenon does not appear in the thick plate, all the four methods can obtain high accuracy and is hard to distinguish which is higher. However, for the thin plate, the difference in the accuracy of the four methods is obvious. The accuracy of FEM-DSG and NS-DGS is lower, and both NS-FEM and the proposed method can achieve high accuracy compared with the reference result.

4.2. Free Vibration Analysis. In this section, numerical examples of free vibration for various plates are given. The nondimensional frequency parameter is normalized by $\lambda = (\omega a^2 \sqrt{\rho t / D})^{1/2}$ [35], where ω is the circle frequency value, a is the geometry size given in each problem, ρ is the mass density, t is the thickness, and $D = Et^3 / (12(1 - \nu^2))$ is the bending stiffness.

4.2.1. Square Plates. Square plates of length a , width b , and thickness t are considered. The material parameters are

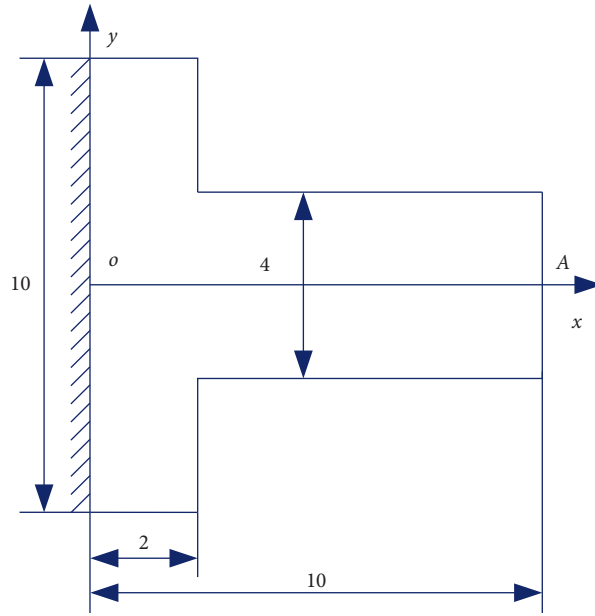


FIGURE 6: Geometry illustration of a T-plate.

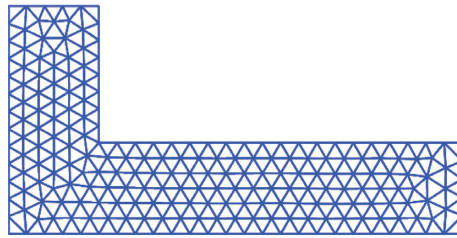


FIGURE 7: Domain discretization using triangular.

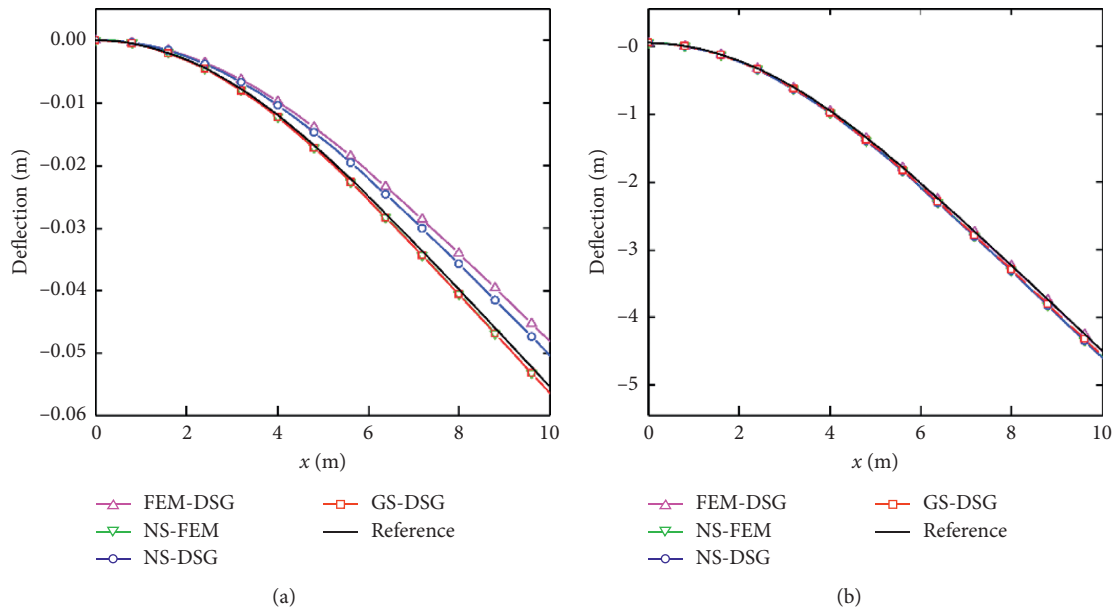


FIGURE 8: Deflections along the line OA with different thickness (uniformly distributed load): (a) $t = 0.01$; (b) $t = 0.5$.

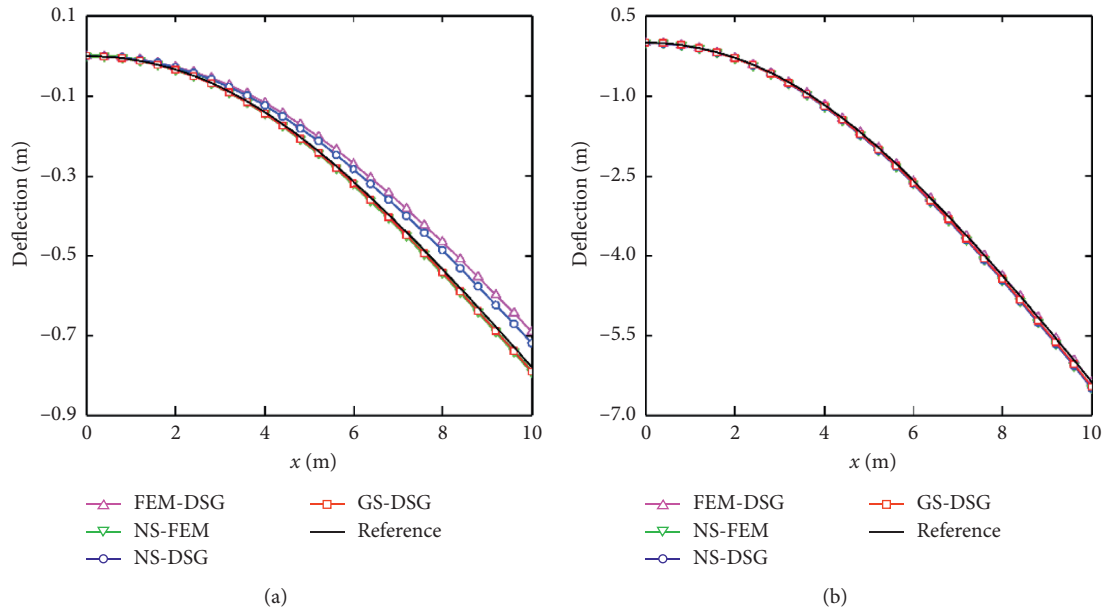


FIGURE 9: Deflections along the line OA with different thickness (concentrated load): (a) $t = 0.01$; (b) $t = 0.5$.

$E = 2.0 \times 10^{11}$, $\nu = 0.3$, and $\rho = 8000$. The plate is modeled with uniform meshes of 4, 8, 16, and 24 elements each side. The boundary conditions are simply supported (S), clamped (C), and free (F). SSSS means that all four sides are simply supported, and the others are similar.

First, the SSSS plate corresponding to length-to-width ratios $a/b = 1$ is considered. The thickness-to-length for the thin plate is $t/a = 0.005$ and for the thick plate is $t/a = 0.1$, respectively. Figures 10(a), 10(c), and 10(d) show the geometry of the plate and its mesh grid, respectively. Table 2 shows the values of the nondimensional frequency parameter λ corresponding to the six frequencies using 4×4 , 8×8 , 16×16 , and 24×24 meshes. It is observed that the accuracy of the presented method increases with the decreasing size of the mesh elements, and the results of GS-DSG agree well with the analytical ones. For the same mesh, the presented method is more accurate than FEM-DSG, NS-FEM, and NS-DSG elements for both thin and thick plates. Table 3 shows four methods for the first six modes under the 16×16 mesh. The spurious nonzero energy mode is marked with the blue wireframe. It can be clearly found in the table that NS-FEM has spurious nonzero energy modes, that is, severe time instability. The mode obtained by the NS-DSG method cannot eliminate spurious nonzero energy modes completely even using the discrete shear gap technology. In contrast, the advantage of the GS-DSG method is particularly obvious, and there are no spurious nonzero energy modes, which indicates its stability in the time domain.

The second problem is that the mesh of CCCC square plate as shown in Figure 10(b) is the same as that of the SSSS plate. The nondimensional frequency parameter λ corresponding to the first six frequencies of the CCCC plate is shown in Table 4. The corresponding modes under 16×16 are given in Table 5, and the spurious nonzero energy mode is marked with the blue wireframe. It can be found again that the GS-DSG method is superior to the other three methods.

In this example, we further studied five different boundary conditions: SSSF, SFSF, CCCC, CFCF, and CFSF. In this case, a 16×16 regular mesh is adopted for square plates with different boundary conditions. The square of the nondimensional frequency parameter λ corresponding to the first four lowest frequencies is shown in Table 6. As a result, the GS-DSG method is almost superior to the other three methods and is consistent with the exact solution of all frequencies in this problem.

4.2.2. Elliptical Plate. In this section, a simply supported elliptical plate is considered. The geometric parameters of the plate are shown in Figure 11 with thickness $t = 0.5$. The material properties are $E = 2.0 \times 10^{11}$, $\nu = 0.3$, and $\rho = 8000$. Since the analytical solution is unavailable for this problem, the result calculated by the ABAQUS software with a very fine mesh (33345 nodes) is employed as a reference.

To illustrate the benefits of triangular grids, we use an unstructured mesh layout with 446 nodes, as shown in Figure 12. The first 12 natural modes solved by the proposed method are plotted in Table 7. The spurious nonzero energy modes are marked by the blue border, which indicates that the NS-FEM method has the time instability problem. The natural frequencies corresponding to the modes together with other three method solutions are listed in Table 8. Natural frequencies marked by a black border in Table 8 denote the spurious nonzero modes. The relative errors of natural frequencies solved by GS-DSG together with solutions obtained using other three methods are plotted in Figure 13. The following conclusions can be drawn from the results: (1) the results obtained by GS-DSG calculation have no spurious nonzero energy modes and therefore no temporal instability problem; (2) the natural frequencies obtained using the FEM-DSG method are all higher than the reference solutions, with accuracy severely decreasing with

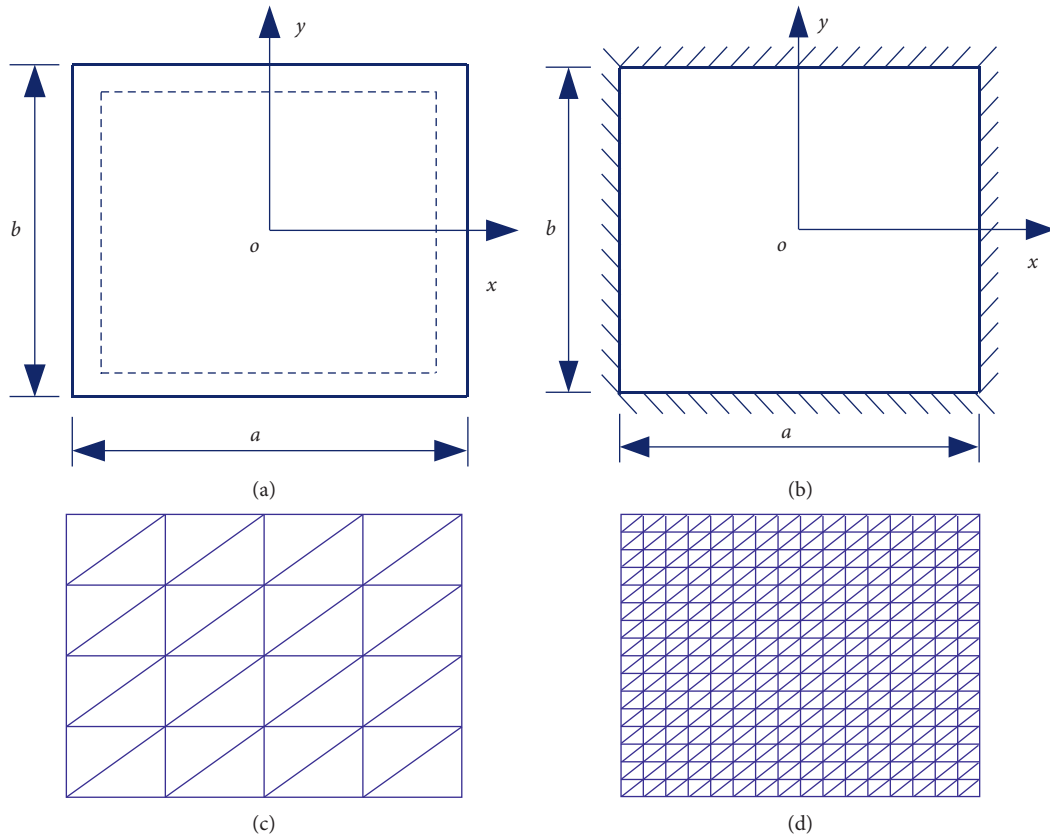


FIGURE 10: (a) Supported plate, (b) clamped plate, and (c, d) triangular meshes.

TABLE 2: A nondimensional frequency parameter λ of an SSSS plate ($a/b = 1$).

t/a	Method	Mode sequence number					
		1	2	3	4	5	6
0.005	FEM-DSG	4.8067	8.5038	9.2631	12.3353	16.6573	17.9400
		4.5190	7.3529	7.5123	9.7058	11.2071	11.2798
		4.4545	7.0943	7.1344	9.0748	10.2148	10.2180
		4.4440	7.0499	7.0680	8.9591	10.0481	10.0521
	NS-FEM	3.8523	4.6180	4.6696	5.4803	5.5805	5.7068
		4.2873	4.7464	4.9528	5.4243	5.9702	6.2474
		4.3931	4.8182	4.8238	5.2862	5.8463	6.1054
		4.4156	4.7659	4.7660	5.4864	6.2891	6.2921
	NS-DSG	4.1952	6.2489	6.3781	7.4032	7.5154	8.2944
		4.3191	6.7445	6.7573	8.4370	9.3131	9.3758
		4.3853	6.9234	6.9248	8.7009	9.7366	9.7462
		4.4053	6.9658	6.9667	8.7753	9.8308	9.8348
	GS-DSG	4.2893	6.7888	6.9313	8.3816	9.5817	9.6035
		4.3637	6.8888	6.8966	8.6707	9.6991	9.7403
		4.4101	6.9687	6.9729	8.7846	9.8260	9.8393
		4.4228	6.9918	6.9945	8.8249	9.8738	9.8807
	Reference [72]	4.443	7.025	7.025	8.886	9.935	9.935

TABLE 2: Continued.

t/a	Method	Mode sequence number					
		1	2	3	4	5	6
0.1	FEM-DSG	4.6700	7.9713	8.5811	10.3261	10.6011	10.6017
		4.3964	6.9971	7.1328	8.9615	9.7532	10.1849
		4.3200	6.7565	6.7874	8.4201	9.4119	9.4185
		4.3012	6.7086	6.7216	8.3093	9.2733	9.2794
		3.7366	4.4102	4.4397	5.1403	5.2270	5.3701
	NS-FEM	4.1438	4.4389	4.5862	5.0152	5.4576	5.6616
		4.2327	4.4534	4.4553	4.8923	5.3434	5.5359
		4.2534	4.4057	4.4058	5.0280	5.6971	5.6991
		4.1026	5.9418	6.0366	6.7521	6.7843	7.1540
		4.2175	6.4611	6.4728	7.3821	7.6795	7.7982
	NS-DSG	4.2675	6.6158	6.6158	7.6205	7.8446	7.8451
		4.2759	6.6439	6.6458	7.7018	7.8603	7.8604
		4.1863	6.4643	6.5416	7.7482	8.5051	8.6428
		4.2546	6.5859	6.5877	8.0866	8.9413	8.9637
		4.2816	6.6463	6.6487	8.1817	9.0967	9.0979
	GS-DSG	4.2830	6.6576	6.6593	8.2002	9.1314	9.1365
		Reference [72]	4.37	6.74	6.74	8.35	9.22

TABLE 3: First 6 modes of the square plate (SSSS) solved by different methods with 16×16 meshes.

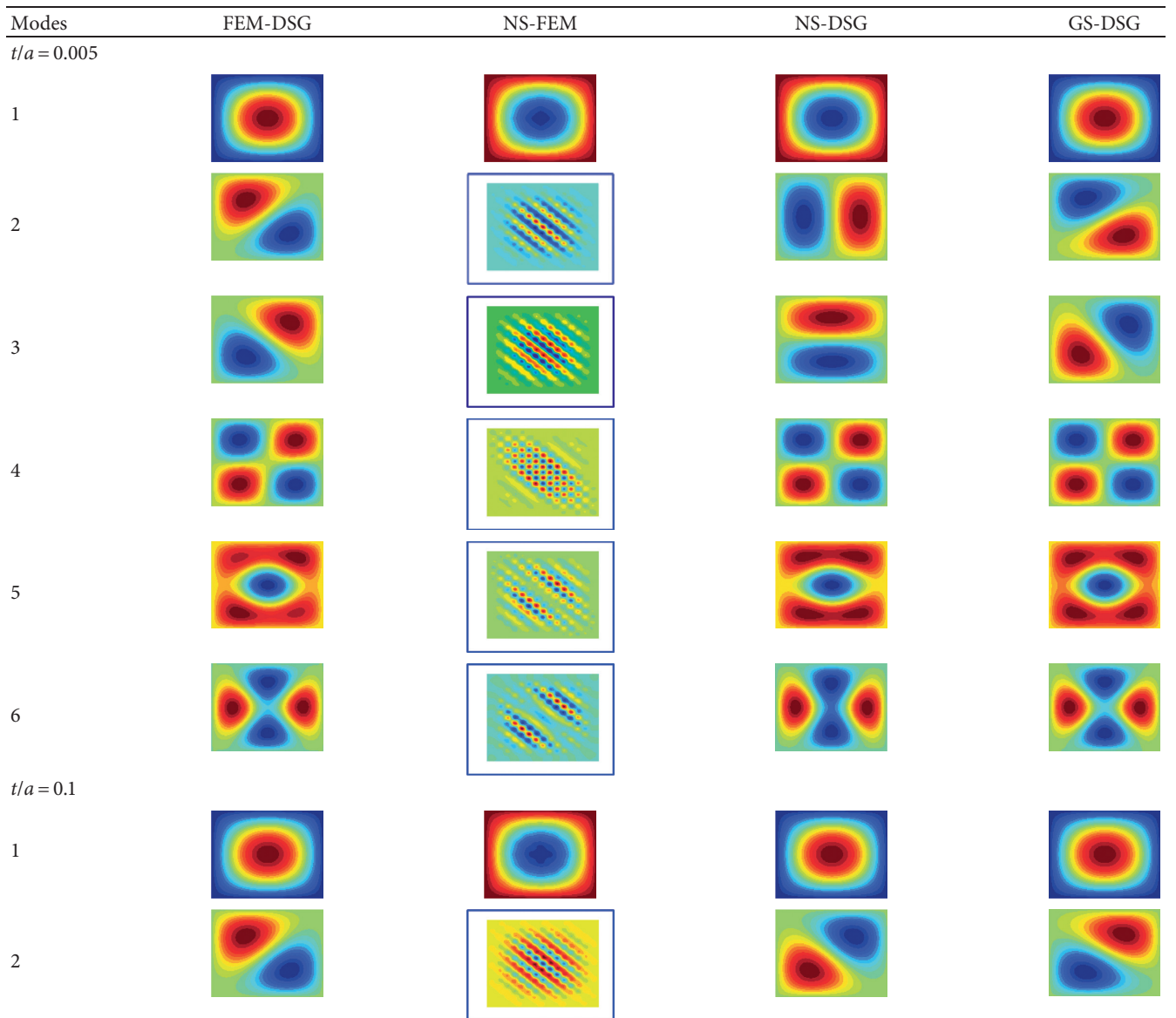


TABLE 3: Continued.

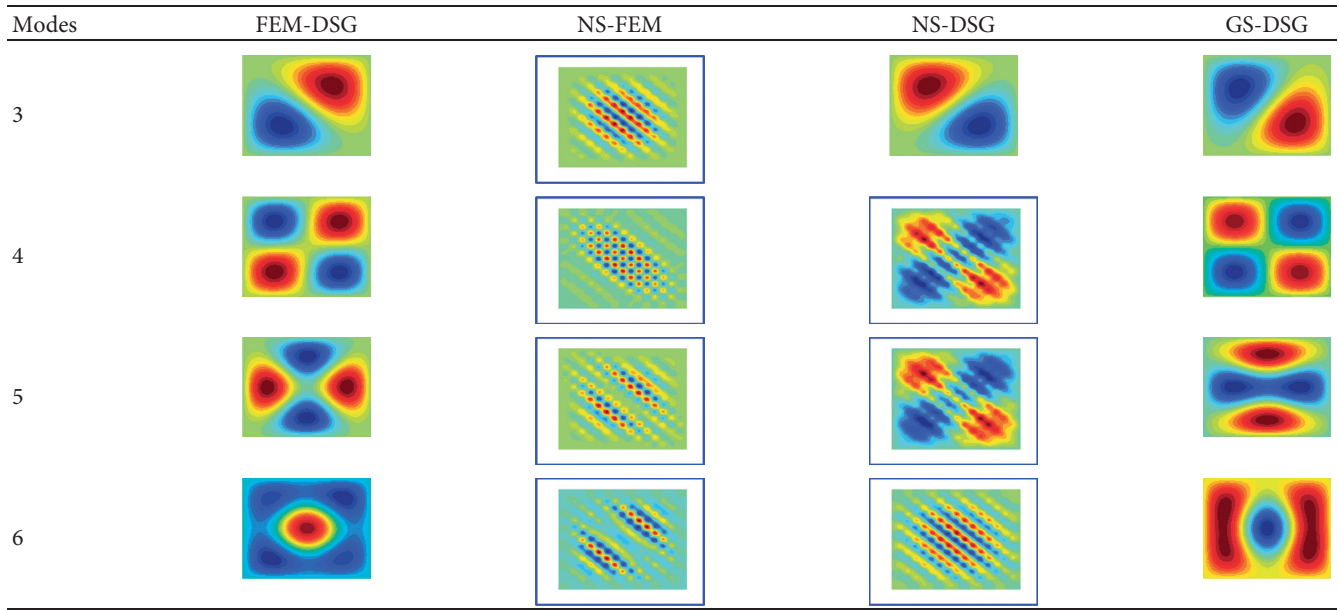


TABLE 4: A nondimensional frequency parameter λ of a CCCC plate ($a/b = 1$).

t/a	Method	Mode sequence number					
		1	2	3	4	5	6
0.005	FEM-DSG	8.6743	14.6071	18.4781	22.1215	28.3891	29.1794
		6.3839	9.4693	9.7732	12.4103	13.8892	14.2365
		6.0740	8.7422	8.8097	10.8089	11.9473	11.9823
		6.0284	8.6355	8.6554	10.5653	11.6629	11.6897
	NS-FEM	4.8662	27.2994	27.4030	30.5485	31.2468	33.7182
		5.5113	5.6369	5.6908	6.1573	6.7345	6.8578
		5.1463	5.1567	5.6597	5.8989	6.2153	6.5428
		4.9637	4.9639	5.7411	5.9520	6.5102	6.5153
	NS-DSG	6.2399	7.7833	14.5143	16.8787	18.5504	19.4584
		8.8488	8.0945	8.2608	9.9613	10.4157	10.8271
		5.9356	8.3981	8.4178	10.1743	11.1144	11.1576
		5.9660	8.4810	8.4879	10.2770	11.2890	11.3201
	GS-DSG	7.1391	10.4788	14.7362	17.0639	18.8060	19.5371
		5.9902	8.4671	8.6174	10.6220	11.2868	11.6486
		5.9694	8.4856	8.5019	10.3112	11.3058	11.3398
		5.9807	8.5191	8.5249	10.3363	11.3724	11.4008
Reference [73]	5.999	8.568	8.568	10.407	11.472	11.498	
0.1	FEM-DSG	7.0255	10.2284	11.3539	11.3850	11.8340	12.8015
		5.9576	8.4011	8.6489	10.3774	11.2084	11.3691
		5.7609	7.9968	8.0525	9.5838	10.4278	10.4803
		5.7274	7.9271	7.9514	9.4369	10.2517	10.2995
	NS-FEM	4.6154	6.3432	6.7867	6.8568	7.0858	7.6405
		4.8119	4.9749	5.3796	5.4743	5.9144	5.9380
		4.5501	4.5572	5.1111	5.5108	5.6206	5.7290
		4.4494	4.4494	5.2545	5.6658	5.7524	5.7533
	NS-DSG	5.7131	7.0630	7.8426	8.2222	8.3801	8.4698
		5.5540	7.4852	7.5508	7.7638	7.9153	8.2500
		5.6544	7.7558	7.7675	7.9294	7.9310	8.0354
		5.6797	7.8190	7.8242	7.9132	7.9133	7.9705
	GS-DSG	6.1305	8.3987	8.9986	10.2059	10.3095	10.3511
		5.6505	7.7377	7.7683	9.2385	9.8542	9.8966
		5.6787	7.8130	7.8225	9.2477	9.9985	10.0421
		5.6902	7.8433	7.8479	9.2831	10.0575	10.1036
Reference [73]	5.71	7.88	7.88	9.33	10.13	10.18	

TABLE 5: First 6 modes of the square plate (CCCC) solved by different methods with 16×16 meshes.

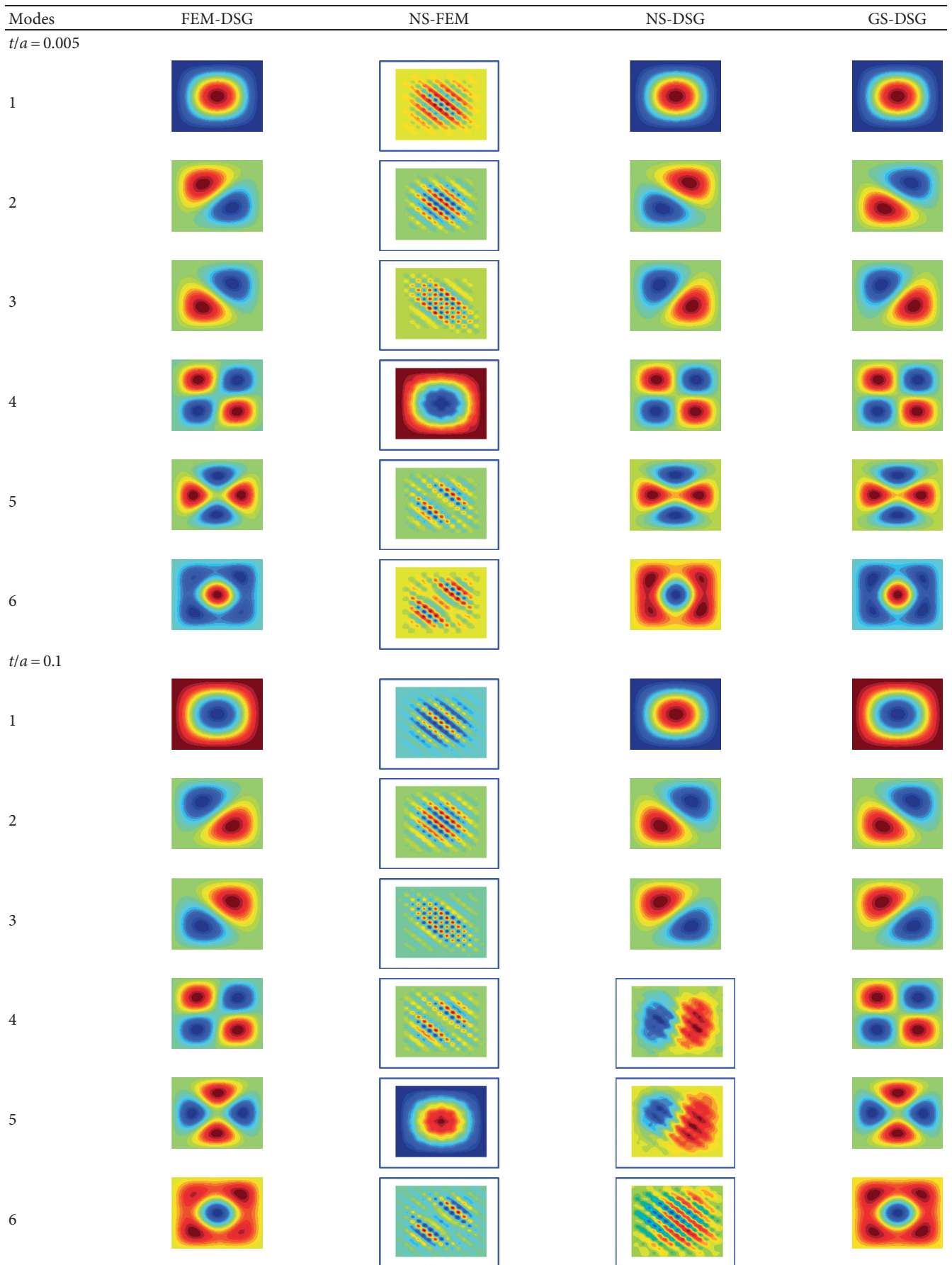


TABLE 6: A nondimensional frequency parameter λ^2 of the square plate (t/a) = 0.005) with various boundary conditions.

Plate type	Method	Mode sequence number			
		1	2	3	4
SSSF	FEM-DSG	11.7066	27.9376	42.1347	60.7093
	NS-FEM	11.5084	23.1688	23.2168	26.8704
	NS-DSG	11.3960	26.6128	40.2935	56.4514
	GS-DSG	11.5498	27.0919	40.7145	57.6083
	Reference [74]	11.685	27.756	41.197	59.066
SFSF	FEM-DSG	9.6797	16.1112	37.0384	39.8117
	NS-FEM	9.5491	15.7288	23.1230	23.1655
	NS-DSG	9.5757	15.2989	34.8264	38.2995
	GS-DSG	9.5996	15.7468	35.4943	38.5924
	Reference [74]	9.631	16.135	36.726	38.945
CCCF	FEM-DSG	24.3065	41.2621	65.6722	80.5606
	NS-FEM	23.4263	25.5865	25.6584	30.8248
	NS-DSG	23.4858	39.0341	60.8599	73.7164
	GS-DSG	23.6981	39.4852	61.9860	74.9583
	Reference [74]	24.020	40.039	63.493	76.761
CFCF	FEM-DSG	22.4444	26.9890	45.1686	63.3315
	NS-FEM	21.7548	24.7811	24.8217	25.7548
	NS-DSG	21.7768	25.8569	42.4465	58.8471
	GS-DSG	21.9631	26.1317	42.9097	59.9521
	Reference [74]	22.272	26.529	43.664	64.466
CFSF	FEM-DSG	15.3251	20.7977	40.5433	50.8558
	NS-FEM	14.9958	20.0826	23.9089	23.9517
	NS-DSG	15.0267	19.8965	38.1048	48.1404
	GS-DSG	15.1039	20.2503	38.7071	48.7522
	Reference [74]	15.285	20.673	39.882	49.500

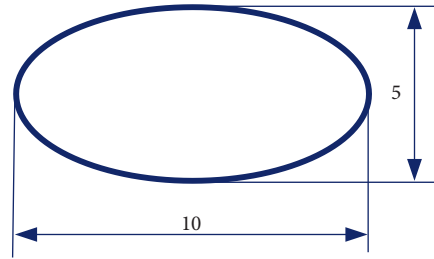


FIGURE 11: Geometric illustration.

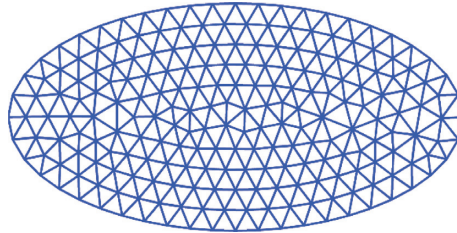


FIGURE 12: Domain discretization.

increasing frequencies; (3) NS-DSG has been improved in the mode calculation of this problem, but its frequency calculation accuracy is still slightly lower than that of GS-DSG. Especially with increasing frequencies, the accuracy of NS-DSG decreases, whereas the presented method maintains accuracy not only for lower frequencies, but also for higher ones; (4) the presented method provides more

accurate natural frequencies than FEM-DSG, NS-FEM, and NS-DSG and can effectively eliminate singular modes.

4.3. Buckling Analysis. In the following examples, we use the proposed method to study the critical buckling load of rectangular plates with different length-width ratios and

TABLE 7: First modes of the elliptical plate solved by different methods.

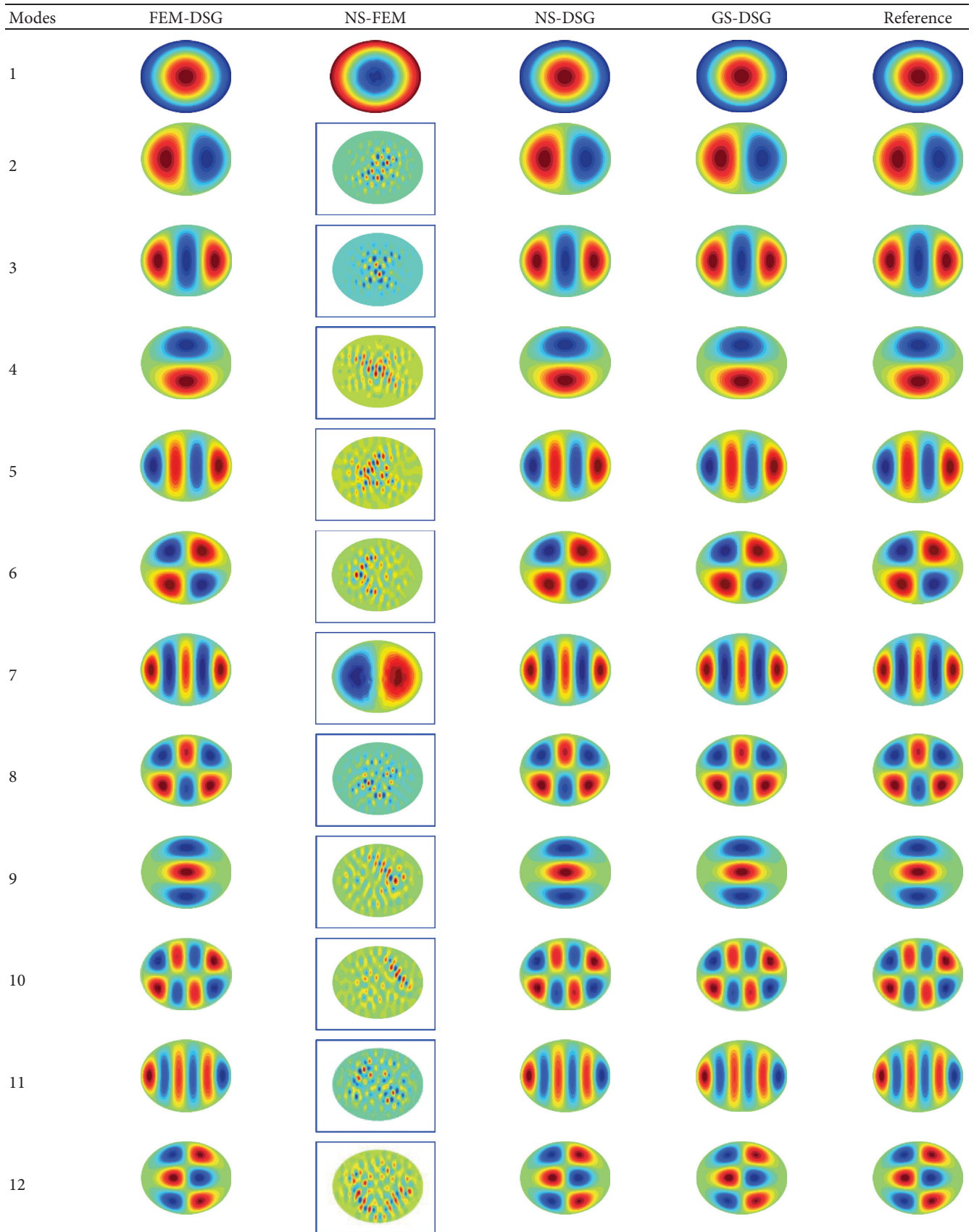


TABLE 8: First 12 parameterized natural frequencies ω of the elliptical plate with 446 nodes.

Modes	FEM-DSG	NS-FEM	NS-DSG	GS-DSG	Reference
1	6.6093	6.3951	6.463	6.4857	6.3595
2	11.938	8.587	11.513	11.572	11.369
3	19.611	9.151	18.496	18.662	18.425
4	23.984	9.579	22.042	22.388	22.203
5	29.916	10.671	27.367	27.782	27.628
6	33.244	10.903	29.873	30.402	30.158
7	43.224	11.273	38.241	39.089	39.012
8	44.833	11.661	39.064	39.934	39.874
9	54.672	13.268	45.674	47.269	47.500
10	59.026	13.963	49.719	51.119	51.421
11	59.871	15.246	50.818	52.405	52.582
12	69.465	15.655	56.690	58.618	58.565

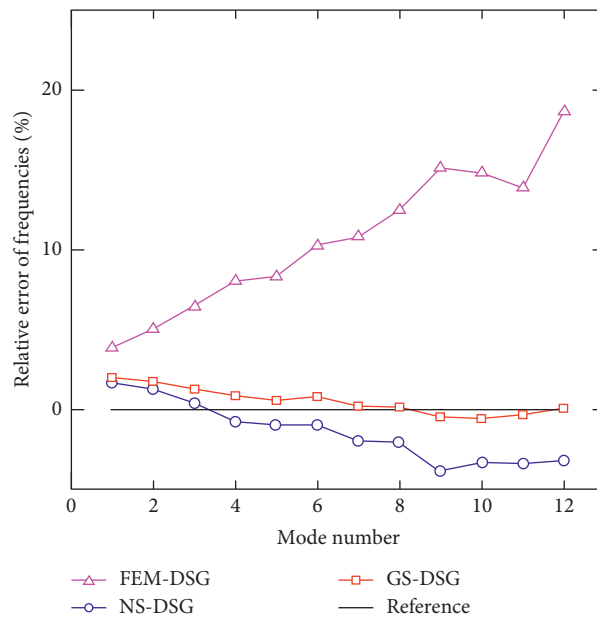


FIGURE 13: Relative errors for the first 12 parameterized natural frequencies of the elliptical plate.

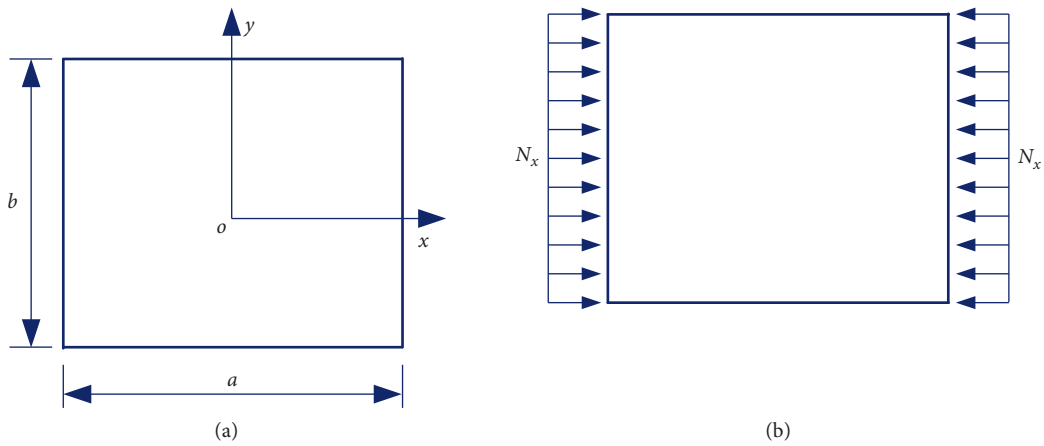


FIGURE 14: Continued.

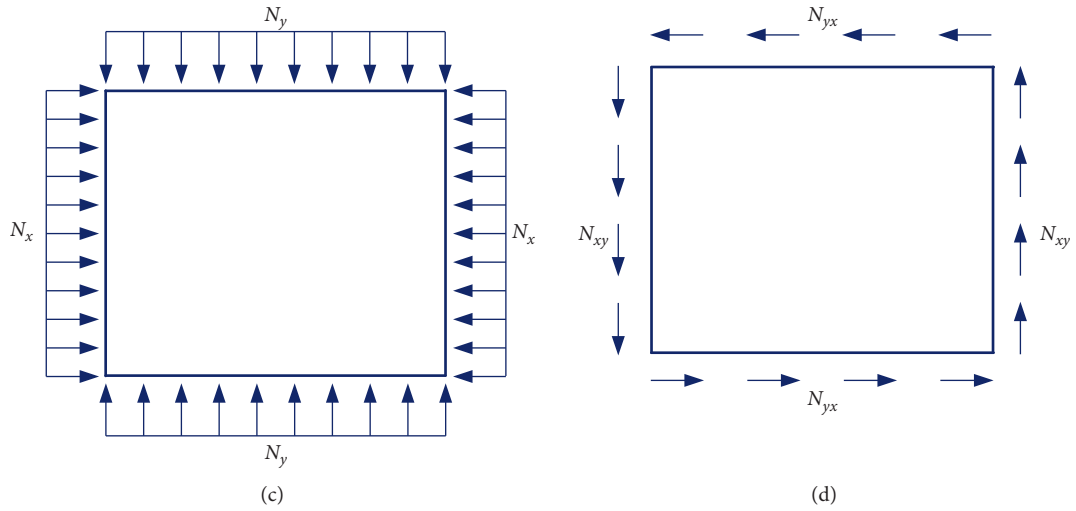


FIGURE 14: Rectangular plates: (a) model; (b) axial compression; (c) biaxial compression; (d) shear in-plane.

TABLE 9: The buckling load factor K of a simply supported rectangular plate with the length-to-width ratio $a/b = 1$, thickness-to-width ratio $t/b = 0.01$, and various loading types.

Load	FEM-DSG	NS-FEM	NS-DSG	GS-DSG	Wang ($\alpha = 0.2$) [40]	Tham [75]	Timoshenko [72]
UC	3.98	3.91	3.88	3.98	3.93	4.00	4.00
BC	1.99	1.96	1.94	1.99	1.96	2.00	2.00
SP	9.29	8.95	9.02	9.37	9.42	9.40	9.33

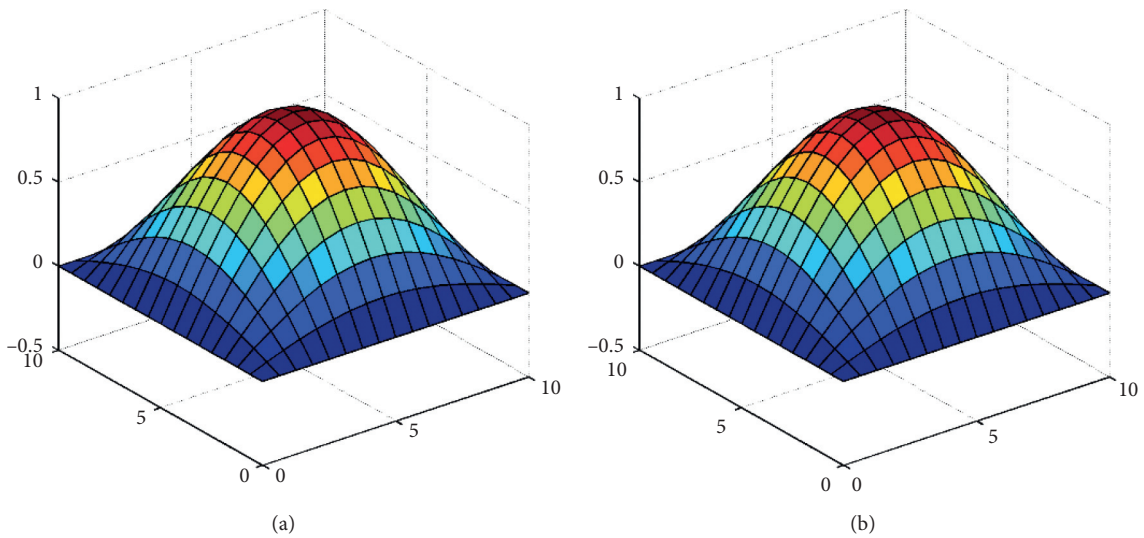


FIGURE 15: Continued.

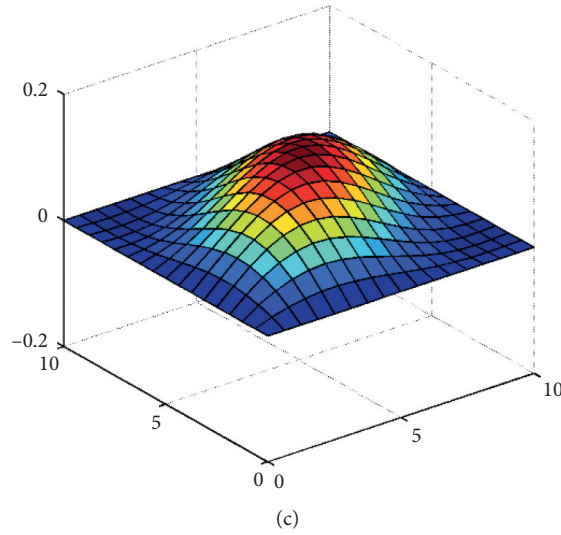


FIGURE 15: The buckling modes of the simply supported square with different types of edge loading: (a) axial compression; (b) biaxial compression; (c) shear in-plane.

TABLE 10: The factor K of axial buckling loads along the x axis of rectangular plates with various length-to-width ratios and various thickness-to-width ratios.

a/b	t/b	FEM-DSG	NS-FEM	NS-DSG	GS-DSG	Meshfree [68]	Pb-2 Ritz [75]	ES-DSG [37]
1.0	0.05	3.8334	3.7167	3.7653	3.8414	3.9293	3.9444	3.9412
	0.1	3.5012	3.3584	3.4637	3.5184	3.7270	3.7865	3.7402
	0.2	2.6379	2.5662	2.6526	2.6839	3.1471	3.2637	3.1263
1.5	0.05	4.1998	4.0422	4.1579	4.2337	4.2116	4.2570	4.2852
	0.1	3.8013	3.6308	3.7871	3.8419	3.8982	4.0250	3.9844
	0.2	2.7879	2.7025	2.8176	2.8490	3.1032	3.3048	3.1461
2.0	0.05	3.8866	3.7597	3.8534	3.9088	3.8657	3.9444	3.9811
	0.1	3.5867	3.4377	3.5717	3.6131	3.6797	3.7865	3.7711
	0.2	2.7672	2.6843	2.7968	2.8143	3.0783	3.2637	3.1415
2.5	0.05	4.0273	3.8801	4.0049	4.0602	3.9600	4.0645	4.1691
	0.1	3.6885	3.5255	3.6827	3.7252	3.7311	3.8683	3.8924
	0.2	2.7918	2.7019	2.8167	2.8445	3.0306	3.2421	3.1234

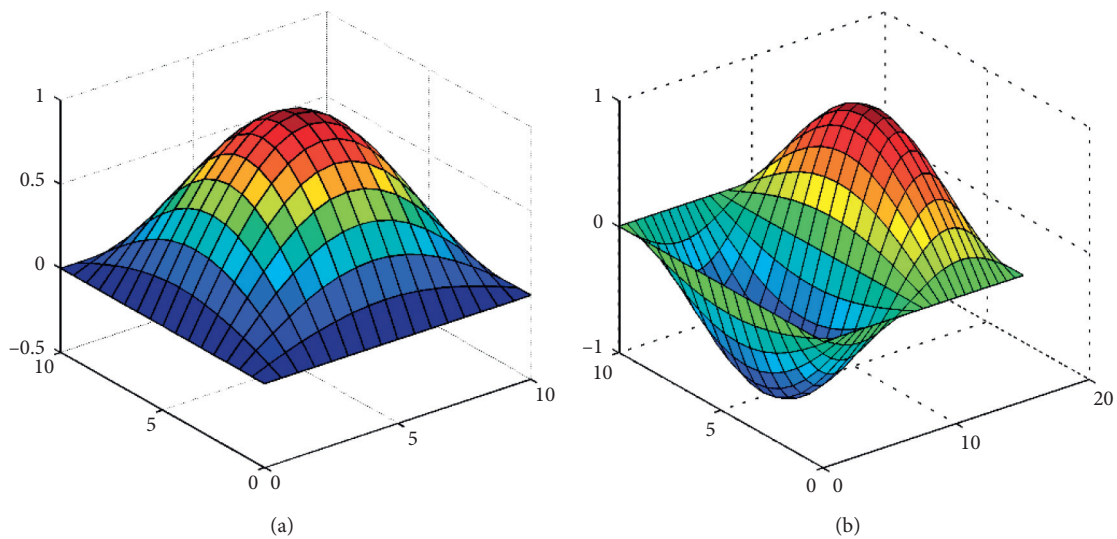


FIGURE 16: Continued.

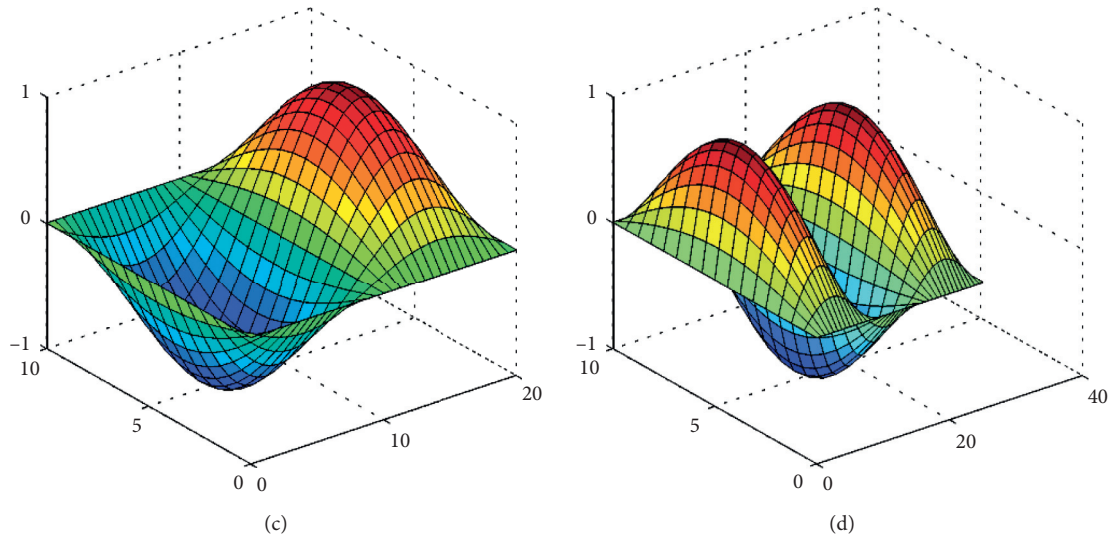


FIGURE 16: Axial buckling modes of simply supported rectangular plates with various length-to-width ratios: (a) $a/b = 1.0$; (b) $a/b = 1.5$; (c) $a/b = 2.0$; (d) $a/b = 2.5$.

different edge loads, as shown in Figure 14. For all cases considered here, the nondimensional buckling load factor is defined as $K = \lambda_{cr} b^2 / (\pi^2 D)$ [35], where the edge width of the plate is expressed as b , the critical buckling load is expressed as λ_{cr} , and the bending stiffness is expressed as D . For the material parameters, $E = 2.0 \times 10^{11}$ and $\nu = 0.3$.

4.3.1. Rectangular Plates Subjected to Different Edge Loading. Firstly, a square plate with thickness t under a simply supported boundary condition is considered. Uniaxial compression (UC), biaxial compression (BC), and shear in-plane (SP) are studied. The problem domain is discretized with a 16×16 uniformly distributed triangular mesh.

The critical buckling load factor K solved using the GS-DSG together with the solutions calculated by FEM-DSG, NS-FEM, and NS-DSG is listed in Table 9. The reference solutions are given by Timoshenko [72], Tham [75], and Wang [40]. From the table, it can be clearly seen that (1) the FEM-DSG and NS-FEM are slightly less accurate than the NS-DSG and GS-DSG due to the resulting overly stiff and soft system, respectively; (2) numerical tests demonstrate that GS-DSG can provide a relatively good accuracy of the critical buckling load factor compared with other three methods. Figure 15 shows the buckling modes of simply supported square plates under different edge loading. It is clear that the results of the GS-DSG can provide very stable buckling modes.

4.3.2. Rectangular Plates with Different Length-to-Width and Thickness-to-Width Ratios. In this section, uniaxial compression rectangular plates with different length-to-width ratios and thickness-to-width ratios are considered. Simply supported boundary conditions are assumed. Four types of length-to-width ratios, $a/b = 1.0, 1.5, 2.0,$ and 2.5 , and three types of thickness-to-width ratios, $t/b = 0.05, 0.1,$ and 0.2 , are

investigated. The problem domain is discretized using a uniformly distributed triangular mesh with 16 elements along the y -axis.

The critical buckling load factors solved by different schemes are given in Table 10. The reference solutions are given by Liew [73], Kitipornchai [74], and Nguyen-Xuan [37]. As in the previous section, the GS-DSG method can obtain very good results compared with other methods. The axial buckling modes of simply supported rectangular plates with thickness-to-width ratios $a/b = 1.0; 1.5; 2.0; 2.5$ are shown in Figure 16. Again, very stable buckling modes can be observed.

5. Conclusions

In this work, a GS-DSG method is formulated for Reissner–Mindlin plate problems in elastic-static, free vibration, and buckling analyses using 3-node triangular elements. The stabilization term is added to the discretized system equations by applying the smoothed Galerkin weak form. Through the formulations and numerical examples, the accuracy of the proposed method is demonstrated. Some concluding remarks can be drawn as follows:

- (1) Several numerical examples indicate that GS-DSG is temporal stable for both free vibration and buckling problems
- (2) In elastic-static analysis, the GS-DSG is free of shear locking and has higher accuracy in the displacement field compared with the FEM-DSG, NS-FEM, and NS-DSG methods
- (3) In free vibration and buckling analyses, the GS-DSG effectively eliminates the spurious nonzero energy modes produced by the original NS-FEM and NS-DSG and provides a relatively accurate prediction of natural frequencies compared with other methods.

Data Availability

The data used to support the findings of this study are available from the corresponding author upon request.

Conflicts of Interest

The authors declare that there are no conflicts of interest regarding the publication of this paper.

Acknowledgments

This work was supported by the National Natural Science Foundation of China under Grant no. 11472137 and the Fundamental Research Funds for the Central Universities under Grant nos. 309181A8801 and 30919011204.

References

- [1] S. Valvano and E. Carrera, "Multilayered plate elements with node-dependent kinematics for the analysis of composite and sandwich structures," *Facta Universitatis, Series: Mechanical Engineering*, vol. 15, no. 1, pp. 1–30, 2017.
- [2] W. Li, Z. X. Gong, Y. B. Chai et al., "Hybrid gradient smoothing technique with discrete shear gap method for shell structures," *Computers & Mathematics with Applications*, vol. 74, no. 8, pp. 1826–1855, 2017.
- [3] K.-U. Bletzinger, M. Bischoff, and E. Ramm, "A unified approach for shear-locking-free triangular and rectangular shell finite elements," *Computers & Structures*, vol. 75, no. 3, pp. 321–334, 2000.
- [4] S. Li, J. Zhang, and X. Cui, "Nonlinear dynamic analysis of shell structures by the formulation based on a discrete shear gap," *Acta Mechanica*, vol. 230, no. 10, pp. 3571–3591, 2019.
- [5] G. Yang, D. Hu, X. Han, and G. Ma, "An extended edge-based smoothed discrete shear gap method for free vibration analysis of cracked Reissner-Mindlin plate," *Applied Mathematical Modelling*, vol. 51, pp. 477–504, 2017.
- [6] K. Y. Size and D. Zhu, "A quadratic assumed natural strain shell curved triangular element," *Computer Methods in Applied Mechanics in Engineering*, vol. 174, pp. 57–71, 1999.
- [7] J. H. Kim and Y. H. Kim, "Three-node macro triangular shell element based on the assumed natural strains," *Computational Mechanics*, vol. 29, no. 6, pp. 441–458, 2002.
- [8] J. Videla, S. Natarajan, and S. P. A. Bordas, "A new locking-free polygonal plate element for thin and thick plates based on Reissner-Mindlin plate theory and assumed shear strain fields," *Computers & Structures*, vol. 220, pp. 32–42, 2019.
- [9] E. D. L. Pugh, E. Hinton, and O. C. Zienkiewicz, "A study of quadrilateral plate bending elements with 'reduced' integration," *International Journal for Numerical Methods in Engineering*, vol. 12, no. 7, pp. 1059–1079, 1978.
- [10] T. Belytschko, H. Stolarski, and N. Carpenter, "AC0 triangular plate element with one-point quadrature," *International Journal for Numerical Methods in Engineering*, vol. 20, no. 5, pp. 787–802, 1984.
- [11] G. S. Dhatt, "An efficient triangular shell element," *AIAA Journal*, vol. 8, no. 11, pp. 2100–2102, 1970.
- [12] J. C. Simo and M. S. Rifai, "A class of mixed assumed strain methods and the method of incompatible modes," *International Journal for Numerical Methods in Engineering*, vol. 29, no. 8, pp. 1595–1638, 1990.
- [13] K.-J. Bathe and E. N. Dvorkin, "A formulation of general shell elements—the use of mixed interpolation of tensorial components," *International Journal for Numerical Methods in Engineering*, vol. 22, no. 3, pp. 697–722, 1986.
- [14] Y. Ko, P.-S. Lee, and K.-J. Bathe, "A new 4-node MITC element for analysis of two-dimensional solids and its formulation in a shell element," *Computers & Structures*, vol. 192, pp. 34–49, 2017.
- [15] D. Chapelle and I. P. Suarez, "Detailed reliability assessment of triangular MITC elements for thin shells," *Computers and Structures*, vol. 86, no. 23–24, pp. 2192–2202, 2008.
- [16] P. S. Lee and K. J. Bathe, "Development of MITC isotropic triangular shell finite elements," *Computers and Structures*, vol. 82, no. 11–12, pp. 945–962, 2004.
- [17] D. Marinkovic, G. Rama, and M. Zehn, "Abaqus implementation of a corotational piezoelectric 3-node shell element with drilling degree of freedom," *Facta Universitatis-Series Mechanical Engineering*, vol. 17, pp. 269–283, 2019.
- [18] O. C. Zienkiewicz and R. L. Taylor, *The Finite Element Method*, Butterworth-heinemann, Oxford, UK, 5th edition, 2000.
- [19] T. J. R. Hughes, *The Finite Element Method: Linear Static and Dynamic Finite Element Analysis*, Prentice-Hall, New York, NY, USA, 2000.
- [20] X. You, W. Li, and Y. Chai, "A truly meshfree method for solving acoustic problems using local weak form and radial basis functions," *Applied Mathematics and Computation*, vol. 365, no. 15, p. 124694, 2020.
- [21] R. A. Gingold and J. J. Monaghan, "Smoothed particle hydrodynamics: theory and application to non-spherical stars," *Monthly Notices of the Royal Astronomical Society*, vol. 181, no. 3, pp. 375–389, 1977.
- [22] B. Nayroles, G. Touzot, and P. Villon, "Generalizing the finite element method: diffuse approximation and diffuse elements," *Computational Mechanics*, vol. 10, no. 5, pp. 307–318, 1992.
- [23] T. Belytschko, Y. Y. Lu, and L. Gu, "Element-free Galerkin methods," *International Journal for Numerical Methods in Engineering*, vol. 37, no. 2, pp. 229–256, 1994.
- [24] W. K. Liu, S. Jun, and Y. F. Zhang, "Reproducing kernel particle methods," *International Journal for Numerical Methods in Fluids*, vol. 20, no. 8–9, pp. 1081–1106, 1995.
- [25] C. A. Duarte and J. T. Odent, "Hp-clouds- an h-p meshless method," *Numerical Methods for Partial Differential Equations*, vol. 12, no. 6, pp. 673–705, 1996.
- [26] S. N. Atluri and T. Zhu, "A new meshless local Petrov-Galerkin (MLPG) approach in computational mechanics," *Computational Mechanics*, vol. 22, no. 2, pp. 117–127, 1998.
- [27] G. R. Liu and Y. T. Gu, "A point interpolation method for two-dimensional solids," *International Journal for Numerical Methods in Engineering*, vol. 50, no. 4, pp. 937–951, 2001.
- [28] T. Rabczuk, T. Belytschko, and S. P. Xiao, "Stable particle methods based on Lagrangian kernels," *Computer Methods in Applied Mechanics and Engineering*, vol. 193, no. 12–14, pp. 1035–1063, 2004.
- [29] Y. Liu, Y. C. Hon, and K. M. Liew, "A meshfree Hermite-type radial point interpolation method for Kirchhoff plate problems," *International Journal for Numerical Methods in Engineering*, vol. 66, no. 7, pp. 1153–1178, 2006.
- [30] P. Krysl and T. Belytschko, "Analysis of thin shells by the element-free Galerkin method," *International Journal of Solids and Structures*, vol. 33, no. 20–22, pp. 3057–3080, 1996.
- [31] H. Mousavi, M. Azhari, and M. M. Saadatpour, "A novel formulation for static and buckling analysis of plates using

- coupled element free Galerkin-finite strip (EFG-FS),” *Applied Mathematical Modelling*, vol. 70, pp. 264–284, 2019.
- [32] K. M. Liew, Y. Q. Huang, and J. N. Reddy, “Analysis of general shaped thin plates by the moving least-squares differential quadrature method,” *Finite Elements in Analysis and Design*, vol. 40, no. 11, pp. 1453–1474, 2004.
- [33] X. Wang and Z. Yuan, “Buckling analysis of isotropic skew plates under general in-plane loads by the modified differential quadrature method,” *Applied Mathematical Modelling*, vol. 56, pp. 83–95, 2018.
- [34] J. Sladek, V. Sladek, and H. A. Mang, “Meshless LBIE formulations for simply supported and clamped plates under dynamic load,” *Computers & Structures*, vol. 81, no. 16, pp. 1643–1651, 2003.
- [35] D. C. Simkins Jr, S. Li, H. Lu et al., “Reproducing kernel element method. Part IV: globally compatible C^1 ($n-1$) triangular hierarchy,” *Computer Methods in Applied Mechanics and Engineering*, vol. 193, no. 12–14, pp. 1013–1034, 2004.
- [36] H. Nguyen-Xuan, T. Rabczuk, S. Bordas et al., “A smoothed finite element method for plate analysis,” *Computer Methods in Applied Mechanics and Engineering*, vol. 197, no. 13–16, pp. 1184–1203, 2008.
- [37] H. Nguyen-Xuan, G. R. Liu, C. Thai-Hoang et al., “An edge-based smoothed finite element method (ES-FEM) with stabilized discrete shear gap technique for analysis of Reissner–Mindlin plates,” *Computer Methods in Applied Mechanics and Engineering*, vol. 199, no. 9–12, pp. 471–489, 2010.
- [38] X. Y. Cui, G. R. Liu, G. Y. Li et al., “Analysis of plates and shells using an edge-based smoothed finite element method,” *Computational Mechanics*, vol. 45, no. 2-3, pp. 141–156, 2010.
- [39] X. Y. Cui, G. R. Liu, G. Y. Li et al., “A smoothed finite element method (SFEM) for linear and geometrically nonlinear analysis of plates and shells,” *Computing in Science and Engineering*, vol. 28, no. 2, pp. 109–125, 2008.
- [40] G. Wang, X. Y. Cui, and G. Y. Li, “Temporal stabilization nodal integration method for static and dynamic analyses of Reissner–Mindlin plates,” *Computers & Structures*, vol. 152, no. C, pp. 125–141, 2015.
- [41] J. T. Chen, I. L. Chen, K. H. Chen, Y. T. Lee, and Y. T. Yeh, “A meshless method for free vibration analysis of circular and rectangular clamped plates using radial basis function,” *Engineering Analysis with Boundary Elements*, vol. 28, no. 5, pp. 535–545, 2004.
- [42] V. N. Van Do and C.-H. Lee, “Nonlinear analyses of FGM plates in bending by using a modified radial point interpolation mesh-free method,” *Applied Mathematical Modelling*, vol. 57, pp. 1–20, 2018.
- [43] T. Q. Bui and M. N. Nguyen, “A moving Kriging interpolation-based meshfree method for free vibration analysis of Kirchhoff plates,” *Computers and Structures*, vol. 89, no. 3–4, pp. 380–394, 2011.
- [44] T.-V. Vu, A. Khosravifard, M. R. Hematiyan, and T. Q. Bui, “A new refined simple TSDT-based effective meshfree method for analysis of through-thickness FG plates,” *Applied Mathematical Modelling*, vol. 57, pp. 514–534, 2018.
- [45] G. R. Liu, K. Y. Dai, and T. T. Nguyen, “A smoothed finite element method for mechanics problems,” *Computational Mechanics*, vol. 39, no. 6, pp. 859–877, 2007.
- [46] Z. Gong, Y. Chai, W. Li et al., “Coupled analysis of structural–acoustic problems using the cell-based smoothed three-node Mindlin plate element,” *International Journal of Computational Methods*, vol. 13, no. 2, pp. 1–25, 2016.
- [47] Y. Chai, W. Li, G. Liu, Z. Gong, and T. Li, “A superconvergent alpha finite element method (SaFEM) for static and free vibration analysis of shell structures,” *Computers & Structures*, vol. 179, no. 15, pp. 27–47, 2017.
- [48] J.-S. Chen, C.-T. Wu, S. Yoon, and Y. You, “A stabilized conforming nodal integration for Galerkin mesh-free methods,” *International Journal for Numerical Methods in Engineering*, vol. 50, no. 2, pp. 435–466, 2001.
- [49] G. R. Liu, T. Nguyen-Thoi, and K. Y. Lam, “An edge-based smoothed finite element method (ES-FEM) for static, free and forced vibration analyses of solids,” *Journal of Sound and Vibration*, vol. 320, no. 4-5, pp. 1100–1130, 2009.
- [50] G. R. Liu, T. Nguyen-Thoi, H. Nguyen-Xuan, and K. Y. Lam, “A node-based smoothed finite element method (NS-FEM) for upper bound solutions to solid mechanics problems,” *Computers & Structures*, vol. 87, no. 1-2, pp. 14–26, 2009.
- [51] G. R. Liu, “A generalized gradient smoothing technique and the smoothed bilinear form for Galerkin formulation of a wide class of computational methods,” *International Journal of Computational Methods*, vol. 5, no. 2, pp. 199–236, 2008.
- [52] G. R. Liu, “G space theory and a weakened weak (W2) form for a unified formulation of compatible and incompatible methods: Part I theory,” *International Journal for Numerical Methods in Engineering*, vol. 81, no. 9, pp. 1093–1126, 2010.
- [53] Z.-Q. Zhang and G. R. Liu, “Temporal stabilization of the node-based smoothed finite element method and solution bound of linear elastostatics and vibration problems,” *Computational Mechanics*, vol. 46, no. 2, pp. 229–246, 2010.
- [54] G. R. Liu and T. Nguyen-Thoi, *Smoothed Finite Element Methods*, CRC Press, Boca Raton, FL, USA, 2010.
- [55] S. Beissel and T. Belytschko, “Nodal integration of the element-free Galerkin method,” *Computer Methods in Applied Mechanics and Engineering*, vol. 139, no. 1-4, pp. 49–74, 1996.
- [56] Y. Chai, W. Li, T. Li, Z. Gong, and X. You, “Analysis of underwater acoustic scattering problems using stable node-based smoothed finite element method,” *Engineering Analysis with Boundary Elements*, vol. 72, pp. 27–41, 2016.
- [57] J. Bonet and S. Kulasegaram, “Correction and stabilization of smooth particle hydrodynamics methods with applications in metal forming simulations,” *International Journal for Numerical Methods in Engineering*, vol. 47, no. 6, pp. 1189–1214, 2000.
- [58] T. Nagashima, “Node-by-node meshless approach and its applications to structural analyses,” *International Journal for Numerical Methods in Engineering*, vol. 46, no. 3, pp. 341–385, 1999.
- [59] C.-T. Wu, S.-W. Chi, M. Koishi, and Y. Wu, “Strain gradient stabilization with dual stress points for the meshfree nodal integration method in inelastic analyses,” *International Journal for Numerical Methods in Engineering*, vol. 107, no. 1, pp. 3–30, 2016.
- [60] M. A. Puso, J. S. Chen, E. Zywickz, and W. Elmer, “Meshfree and finite element nodal integration methods,” *International Journal for Numerical Methods in Engineering*, vol. 74, no. 3, pp. 416–446, 2008.
- [61] H. Feng, X. Y. Cui, and G. Y. Li, “A stable nodal integration method with strain gradient for static and dynamic analysis of solid mechanics,” *Engineering Analysis with Boundary Elements*, vol. 62, pp. 78–92, 2016.
- [62] Q. Duan and T. Belytschko, “Gradient and dilatational stabilizations for stress-point integration in the element-free Galerkin method,” *International Journal for Numerical Methods in Engineering*, vol. 77, no. 6, pp. 776–798, 2009.
- [63] G. Chen, L. Qian, and J. Ma, “A gradient stable node-based smoothed finite element method for solid mechanics problems,” *Shock and Vibration*, vol. 2019, pp. 1–24, 2019.

- [64] G. R. Liu, T. Nguyen-Thoi, and K. Y. Lam, "A novel alpha finite element method (α FEM) for exact solution to mechanics problems using triangular and tetrahedral elements," *Computer Methods in Applied Mechanics and Engineering*, vol. 197, no. 45-48, pp. 3883-3897, 2008.
- [65] G. Chen, L. Qian, and J. Ma, "A gradient stable node-based smoothed finite element method for solid mechanics problems," *Shock and Vibration*, p. 2019, 2019.
- [66] G. Chen, L. Qian, J. Ma, and Y. Zhu, "Smoothed FE-Meshfree method for solid mechanics problems," *Acta Mechanica*, vol. 229, no. 6, pp. 2597-2618, 2018.
- [67] H. Zhang, G. Chen, L. Qian, and J. Ma, "FE-meshfree QUAD4 element with modified radial point interpolation function for structural dynamic analysis," *Shock and Vibration*, vol. 2019, Article ID 3269276, 23 pages, 2019.
- [68] Q. Duan, B. Wang, X. Gao, and X. Li, "Quadratically consistent nodal integration for second order meshfree Galerkin methods," *Computational Mechanics*, vol. 54, no. 2, pp. 353-368, 2014.
- [69] M. Lyly, R. Stenberg, and T. Vihinen, "A stable bilinear element for the Reissner-Mindlin plate model," *Computer Methods in Applied Mechanics and Engineering*, vol. 110, no. 3-4, pp. 343-357, 1993.
- [70] M. Bischoff and K. U. Bletzinger, "Stabilized DSG plate and shell elements," *Trends in Computational Structural Mechanics*, CIMNE, Barcelona, Spain, 2001.
- [71] F. Wu, G. R. Liu, G. Y. Li, A. G. Cheng, and Z. C. He, "A new hybrid smoothed FEM for static and free vibration analyses of Reissner-Mindlin Plates," *Computational Mechanics*, vol. 54, no. 3, pp. 865-890, 2014.
- [72] S. P. Timoshenko and J. N. Goodier, *Theory of Elasticity*, McGraw-Hill Book Company, PA, USA, 3rd edition, 1970.
- [73] K. M. Liew, J. Wang, T. Y. Ng et al., "Free vibration and buckling analyses of shear-deformable plates based on FSDT meshfree method," *Journal of Sound and Vibration*, vol. 276, no. 3-5, pp. 997-1017, 2004.
- [74] S. Kitipornchai, Y. Xiang, C. M. Wang, and K. M. Liew, "Buckling of thick skew plates," *International Journal for Numerical Methods in Engineering*, vol. 36, no. 8, pp. 1299-1310, 1993.
- [75] L. G. Tham and H. Y. Szeto, "Buckling analysis of arbitrarily shaped plates by spline finite strip method," *Computers & Structures*, vol. 36, no. 4, pp. 729-735, 1990.